Oxygen Transport Ceramic Membranes

Quarterly Report

August-December, 2000

By:

Dr. Sukumar Bandopadhyay
and
Dr. Nagendra Nagabhushana

School of Mineral Engineering
University of Alaska Fairbanks

Issued: January, 2001

University of Alaska Fairbanks
School of Mineral Engineering
Brooks 209
Fairbanks, AK 99775

DISCLAIMER

Executive Summary

Conversion of natural gas to liquid fuels and chemicals is a major goal for the Nation as it enters the 21st Century. Technically robust and economically viable processes are needed to capture the value of the vast reserves of natural gas on Alaska's North Slope, and wean the Nation from dependence on foreign petroleum sources. Technologies that are emerging to fulfill this need are all based syngas as an intermediate. Syngas (a mixture of hydrogen and carbon monoxide) is a fundamental building block from which chemicals and fuels can be derived. Lower cost syngas translates directly into more cost-competitive fuels and chemicals.

The currently practiced commercial technology for making syngas is either steam methane reforming (SMR) or a two-step process involving cryogenic oxygen separation followed by natural gas partial oxidation (POX). These high-energy, capital-intensive processes do not always produce syngas at a cost that makes its derivatives competitive with current petroleum-based fuels and chemicals.

In the mid 80's BP invented a radically new technology concept that will have a major economic and energy efficiency impact on the conversion of natural gas to liquid fuels, hydrogen, and chemicals.[1] This technology, called Electropox, integrates oxygen separation with the oxidation and steam reforming of natural gas into a single process to produce syngas with an economic advantage of 30 to 50 percent over conventional technologies.[2]

The Electropox process uses novel and proprietary solid metal oxide ceramic oxygen transport membranes [OTMs], which selectively conduct both oxide ions and electrons through their lattice structure at elevated temperatures.[3] Under the influence of an oxygen partial pressure gradient,

---

[1]Mazanec, T. J.; Cable, T. L.; Frye, J. G., Jr.; US 4,793,904, 27 Dec **1988**, assigned to The Standard Oil Company (now BP America), Mazanec, T. J.; Cable, T. L.; US 4,802,958, 7 Feb **1989**, assigned to the Standard Oil Co. (now BP America), Cable, T. L.; Mazanec, T. J.; Frye, J. G., Jr.; European Patent Application 0399833, 24 May **1990**, published 28 November **1990.**

[2]Bredesen, R.; Sogge, J.; "A Technical and Economic Assessment of Membrane Reactors for Hydrogen and Syngas Production" presented at Seminar on the Ecol. Applic. of Innovative Membrane Technology in the Chemical Industry", Cetraro, Calabria, Italy, 1-4 May **1996**.

[3]Mazanec, T.J., *Interface*, **1996**; Mazanec, T.J., *Solid State Ionics*, 70/71, **1994** 11-19; "Electropox: BP's Novel Oxidation Technology", T.J. Mazanec, pp 212-225, in "The Role of Oxygen in Improving Chemical Processes", M. Fetizon and W.J. Thomas, eds, Royal Society of Chemistry, London, **1993**; "Electropox: BP's Novel Oxidation Technology", T.J. Mazanec, pp 85-96, in "The Activation of Dioxygen and Homogeneous Catalytic Oxidation", D.H.R. Barton, A. E. Martell, D.T. Sawyer, eds, Plenum Press, New York, **1993**; "Electrocatalytic Cells for Chemical Reaction", T.J. Mazanec, T.L. Cable, J.G. Frye, Jr.; Prep Petrol Div ACS, San Fran, **1992** *37*, 135-146; T.J. Mazanec, T.L. Cable, J.G. Frye, Jr.; *Solid State Ionics*, **1992**, 53-56, 111-118.

oxygen ions move through the dense, nonporous membrane lattice at high rates with 100 percent selectivity. Transported oxygen reacts with natural gas on the fuel side of the ceramic membrane in the presence of a catalyst to produce syngas.

In 1997 BP entered into an OTM Alliance with Praxair, Amoco, Statoil and Sasol to advance the Electropox technology in an industrially sponsored development program. These five companies have been joined by Phillips Petroleum and now are carrying out a multi-year $40+ million program to develop and commercialize the technology. The program targets materials, manufacturing and engineering development issues and culminates in the operation of semi-works and demonstration scale prototype units.

The Electropox process represents a truly revolutionary technology for conversion of natural gas to synthesis gas not only because it combines the three separate unit operations of oxygen separation, methane oxidation and methane steam reforming into a single step, but also because it employs a chemically active ceramic material in a fundamentally new way. On numerous fronts the commercialization of Electropox demands solutions to problems that have never before been accomplished. Basic problems in materials and catalysts, membrane fabrication, model development, and reactor engineering all need solutions to achieve commercial success.

Six important issues have been selected as needing understanding on a fundamental level at which the applied Alliance program cannot achieve the breadth and depth of understanding needed for rapid advancement. These issues include

1. Oxygen diffusion kinetics (University of Houston)
2. Grain structure and atomic segregation (University of Illinois - Chicago)
3. Phase stability and stress development (University of Missouri - Rolla)
4. Mechanical property evaluation in thermal and chemical stress fields (University of Alaska Fairbanks)
5. Graded ceramic/metal seals (Massachusetts Institute of Technology)

Statement of Work

Task 1   Design, fabricate and evaluate ceramic to metal seals based on graded ceramic powder / metal braze joints.

Task 2   Evaluate the effect of defect configuration on ceramic membrane conductivity and long term chemical and structural stability.

Task 3   Determine materials mechanical properties under conditions of high temperatures and reactive atmospheres.

Task 4   Evaluate phase stability and thermal expansion of candidate perovskite membranes and develop techniques to support these materials on porous metal structures.

Task 5   Assess the microstructure of membrane materials to evaluate the effects of vacancy-impurity association, defect clusters, and vacancy-dopant association on the membrane performance and stability.

Task 6   Measure kinetics of oxygen uptake and transport in ceramic membrane materials under commercially relevant conditions using isotope labeling techniques.

This is the third quarterly report on oxygen Transport Ceramic Membranes. In the following, the report describes the progress made by our university partners in Tasks 1 through 6, experimental apparatus that was designed and built for various tasks of this project, thermodynamic calculations, where applicable and work planned for the future.

Task 1 & 2 Development of Ceramic Membrane/Metal Joints

Prof. Thomas W. Eagar, Dr Harold R Larson,
Mr Raymundo Arroyave and Ms Jocelyn L. Wiese

ABSTRACT

This is the fifth quarterly report on a new study to develop a ceramic membrane/metal joint. Results of wetting experiments on commercially available Nickel based brazing alloys on perovskite surfaces are described. Additionally, experimental and numerical investigations on the strength of concentric ceramic/metal joints are presented.

Development of Ceramic-Metal Seal

Preliminary experiments using La-Sr-Cr-O discs

The previous status report discussed experiments performed using ceramic oxygen membrane ($La_{.6}Sr_{.4}FeO_3$) and Haynes 230® discs. The first studies, using "conventional" reactive brazing alloys (with titanium or zirconium additions) showed excessive reactivity between the ceramic membrane and the braze. It is suspected that extensive decomposition of the membrane takes place due to the reaction between the reactive element dissolved in the braze and oxygen from the ceramic.

The findings of those experiments can be summarized:
- Ni-based alloys wet the ceramic, however cracks parallel to the ceramic-metal interface were observed in the sample brazed at 10^{-9} atm. No cracking was observed in the sample brazed at 10^{-5} atm.
- There is extensive reaction between the ceramic and braze metal. Most notably, an Fe-depleted zone is formed and Fe "islands" are created in the ceramic. Sr segregates at the interface, and a La-rich layer is in contact with the braze.
- Cracks seem to originate from the Fe-depleted zone.

Wetting experiments on $(La_{.2}Sr_{.8})(Cr_{.2}Fe_{.8})O_3$ disks

Wetting experiments have begun using the $(La_{.2}Sr_{.8})(Cr_{.2}Fe_{.8})O_3$ ceramic oxygen membrane. Wetting experiments were done using commercially available Ni-based brazing alloys (Table 1).

Table 1: Braze Alloy Composition

	Cr	Si	Fe	B	C	Ni
Alloy 1	14%	4.5%	4.5%	3%	0.7%	Bal
Alloy 2	19%	10.2%	--	--	0.03%	Bal
Alloy 3	15%	--	--	3.5%	0.03%	Bal

The experimental procedure was as follows:
- Powdered brazing alloys were deposited on top of the ceramic surfaces using a binding gel.

- When dry, the discs were put in the furnace, and heated up to 750C at a rate of 10C/minute. The discs were held at 750C for 15 minutes and then cooled at 10C/minute.
- The PO2 was 10^{-8} atm.

Alloy 1 was observed to wet the ceramic. However, as the SEM image and composition data (Figure 1) shows, La and Fe-depleted areas were found close to the ceramic / braze interface and La appears to segregate at the interface. This is similar to the phenomena observed for the previous experiments conducted on ($La_{.6}Sr_{.4}FeO_3$) ceramics. It is believed that this excessive reaction between the ceramic material and the braze alloy is detrimental for the final stability of the ceramic/metal interface.
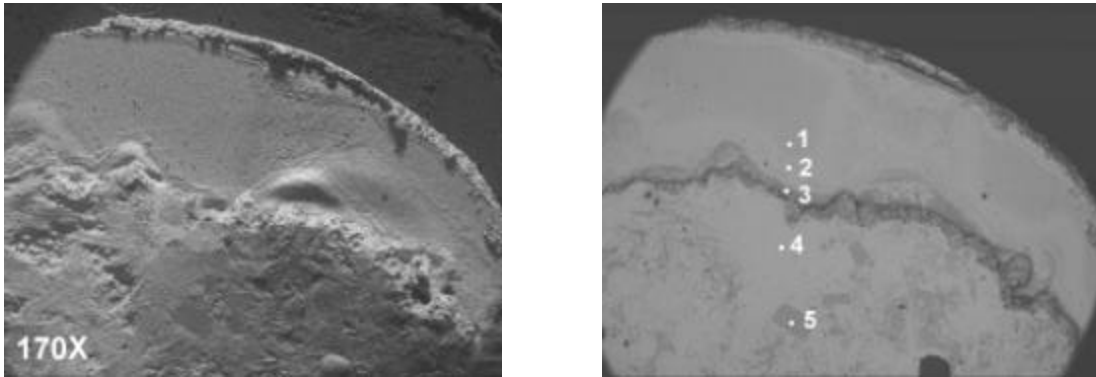

Figure 1: (L) Wetting of Alloy 1 on ceramic surface. (R) EDS data points (Table 2)

Table 2: Composition of points on Alloy 1 / Ceramic interface

	1	2	3	4	5
O	68.30	74.64	58.85	0.00	0.00
Cr	2.98	0.00	5.52	8.09	92.84
Fe	9.69	2.23	4.98	3.93	0.00
Ni	0.46	1.02	14.84	78.28	7.16
Sr	16.58	21.37	14.39	0.00	0.00
La	1.98	0.74	1.42	0.00	0.00
Si	0.00	0.00	0.00	9.70	0.00
B	0.00	0.00	0.00	?	?

The interaction between Alloy 2 and the ceramic is shown in Figure 2 and Table 3. The Cr in the braze metal reacts with the ceramic surface, forming Cr_2O_3. This ceramic layer cannot be wetted by the remaining Si-enriched Ni-based alloy. To decrease the effects of Cr and Si in the braze alloy, the presence of Fe and B is necessary. Using Si as the sole melting point depressant in the brazing alloy apparently is not an optimal solution, since the separation of Cr and its reaction with the perovskite surface is being promoted.
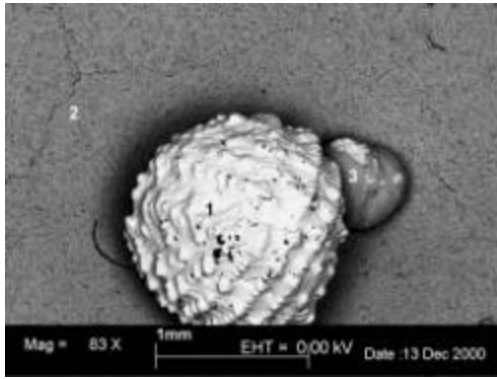
**Table 3: Composition of Alloy 2 / Ceramic interface**

	1	2	3
Ni	64.67	9.24	1.16
Cr	5.11	1.66	30.19
Fe	0.00	8.71	0.27
Si	30.22	0.00	1.65
La	0.00	2.43	0.00
Sr	0.00	9.76	0.00
O	0.00	68.20	66.73

Figure 2: Wetting of Alloy 2 on Ceramic

Alloy 3 was observed to wet the ceramic as well, chemical segregation was again observed in the ceramic (Figure 3, Table 4). La and Fe were depleted in the region close to the braze / ceramic interface. The ceramic in these samples was cracked. The cracking in the ceramic is attributed to the lack of Fe in the braze alloy.

As was observed in the previous experiments presented in the past report, the initiation of cracks in the ceramic side of the ceramic/metal interface is associated with the presence of Fe depleted regions across the interface. As the Fe content in the braze alloy decreases, the Fe in the ceramic tends to diffuse out of the ceramic lattice into the braze material. Therefore, the Fe content in the braze alloy needs to be optimized.

Figure 3: (L) Interaction between Alloy 3 and Ceramic.   (R) EDS data points.
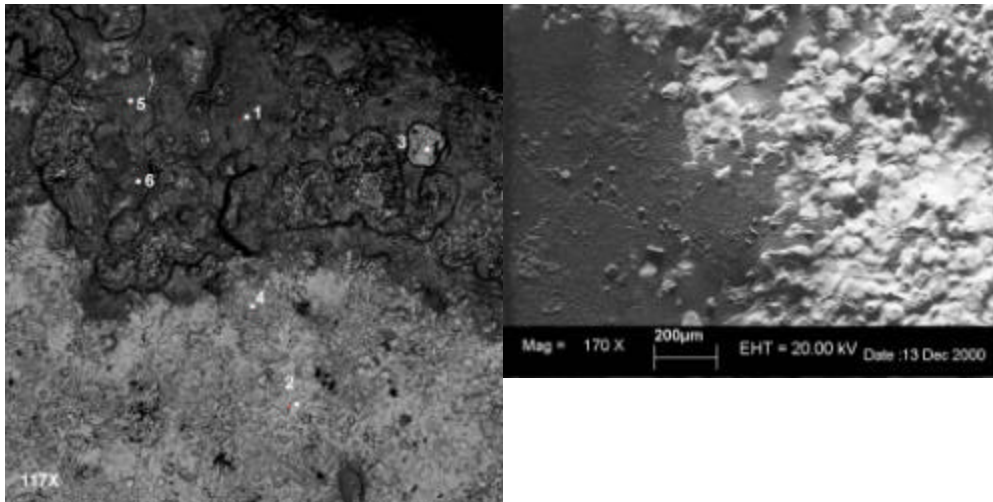
The results of the wetting experiments can be summarized:
- Ni-Cr-Si alloys are not adequate. Cr segregates and reacts with the ceramic to form Cr_2O_3, the remaining Ni-Si de-wets.
- Ni-Cr-B alloys wet the ceramic, however cracking (without externally applied stresses) is observed.
- Ni-Cr-Fe-B alloys are promising, since wetting is observed and the reaction with the ceramic is not as extensive as in the alloys lacking Fe.

3

Table 4: Chemical analysis of Alloy 3/ Ceramic interface

Elements	1	2	3	4	5	6
Ni	5.30	82.23	87.90	22.35	38.86	0.72
Cr	16.29	14.54	4.73	13.18	6.21	18.97
Fe	0.30	2.55	6.08	0.69	2.34	0.13
La	0.13		0.16	0.01	0.18	0.03
Sr	10.23		1.13	0.32	3.92	0.87
O	67.76			63.46	48.49	79.27
B	N/A	N/A	N/A	N/A	N/A	N/A

Future Work

In order to have a more complete understanding of the chemical interactions between Ni-based brazing alloys and perovskites, it is necessary to experiment with custom-made braze alloys with varying compositions of B, Fe, Cr, Si and Ni. By studying their wetting properties, as well as their reactivity, it might be possible to find an optimum alloy for this particular ceramic/metal seal application.

When suitable braze alloys are identified, the strength of the joints made between the oxygen transfer membrane and Haynes 230® will be evaluated.

Mechanical Properties of the Joints

Testing techniques are being developed to measure and understand the mechanical properties of concentric metal-ceramic membrane joints. Since actual perovskite tubes are currently unavailable, we have chosen to study the properties of alumina tubes brazed around nickel- and iron-based alloy rods, using commercially available Ticusil™ brazing alloy. These materials were chosen because the brazing of alumina with this alloy is well documented in the literature, and because the metals represent a wide range of engineering alloys.

We are interested in how the properties of the base metal affect the residual stresses present in the brazed joint. This knowledge will help us design lower-stress joints for the ceramic membrane application. The testing and analytical methods that are being developed will be applied to the "perovskite"/Haynes 230® system once brazing alloys have been developed for those materials and mechanical property data for the ceramic is available.

Table 5: Materials Used in Experiments

Material	Total CTE (ppm/C)		Yield Strength (Mpa)	
	20C	800C	20C	800C
Invar	1	11	175	50
Hastelloy B2	10	13	375	300
Inconel 600	13	15	260	100
304 Stainless Steel	15	18	260	100

| Alumina | 7 | 8.5 | -- | -- |

The geometry of the brazed rod-in-tube samples is shown schematically in Figure 4. The inner diameter of the ceramic tube is 0.257". Two different rod diameters are being used: 0.250" and 0.247", resulting in braze thickness of 3.5 mil and 5 mil respectively. The joint overlap length is being systematically varied between 0.2" and 0.35". Due to the different rates of thermal expansion between the ceramic and base metal, more residual stress should be present in the longer joints. We predict that this residual stress will degrade the shear strength of the joints.
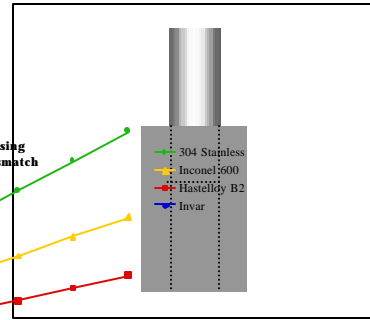
Figure 4 Mechanical tests specimens

Finite Element Models

A series of finite element (FE) models to simulate the residual stresses that develop in the joints during cooling is being constructed using ABAQUS. The axisymmetric model is thermally loaded from 780C (the solidus of Ticusil™ brazing alloy) to room temperature. The elastic strain energy present in the joint after cooling is being used as the residual stress metric. (Strain energy is essentially the integral of the stress over the deformed volume of the part, and elastic strain energy the elastic component of the strain energy).

The model assumes that the ceramic has perfectly elastic[4] behavior and braze alloy has elastic-perfectly plastic[5] behavior. The base metal is being modeled in both the perfectly elastic and elastic-perfectly plastic case, since the actual behavior is likely a mix of the two (work hardening).

The model calculates the total elastic strain energy for each material combination over a range of joint lengths. When the base metal is assumed be perfectly elastic, the total elastic strain energy present in the joint is controlled by the CTE mismatch between the materials (Figure 5R). However, if the metal is assumed to be elastic-perfectly plastic, the yield strength of the material becomes important (Figure 5L). Plastic deformation of the braze metal and base metal can dissipate some of the residual stress, lowering the amount of elastic strain energy present in the joint.

The models back up the hypothesis that the CTE mismatch between materials will result in significant residual stresses, which will likely degrade the mechanical strength of the joint.
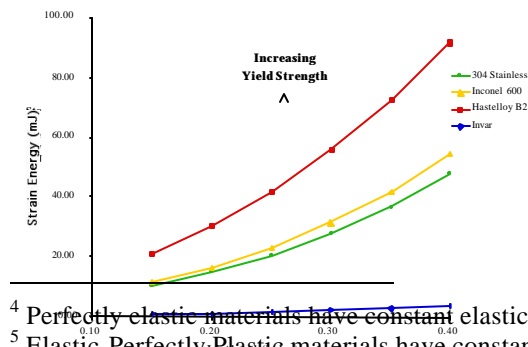
[4] Perfectly elastic materials have constant elastic modulus do not yield
[5] Elastic-Perfectly Plastic materials have constant elastic modulus up to the yield stress; the yield stress does not increase

Figure 5: Total elastic strain energy present in joints after cooling.

(R) Base metal perfectly elastic (L) Base metal elastic-perfectly plastic

Measurement of Interfacial Shear Strength

The shear strength of the joints is measured by loading these samples in compression using an Instron testing machine. If the braze is weaker than the ceramic tube, the joint will fail by shearing the interface, however if the braze is stronger, the ceramic will fracture in compression.

Joints have been successfully made between the alumina and all four base metals and the strength of the joints was measured. Figure 6 shows strength data for all four material combinations at different joint lengths. Two distinct fracture modes were observed in these samples: most of the samples failed ductily at the interface (presumably through the braze) however a few samples failed brittlely in the ceramic. The joints appeared to support maximum load at a joint overlap of 0.25".
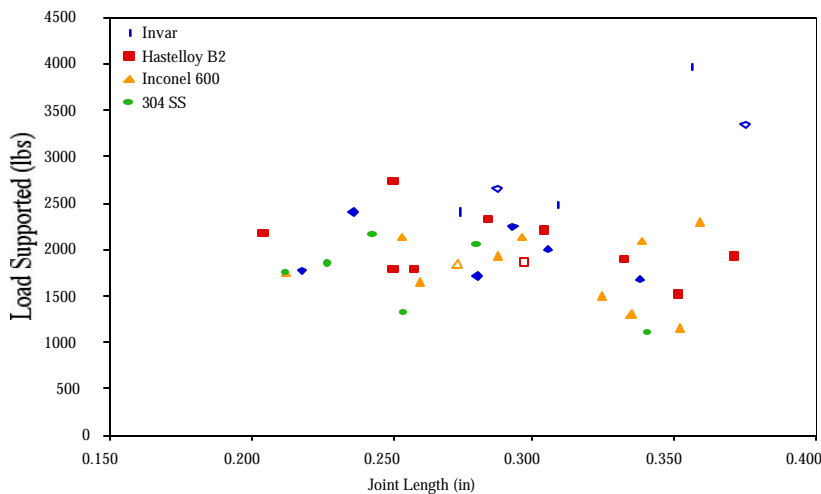
Figure 6: Normalized joint shear strength

The absolute load data can be normalized to the interfacial shear strength by dividing the load supported by brazed joint area. Figure 7 clearly shows that the interfacial shear strength decreases as the joint length increases. A subset of the invar-alumina joints are much stronger than of the other joints, and the reasons for this observation are being investigated.
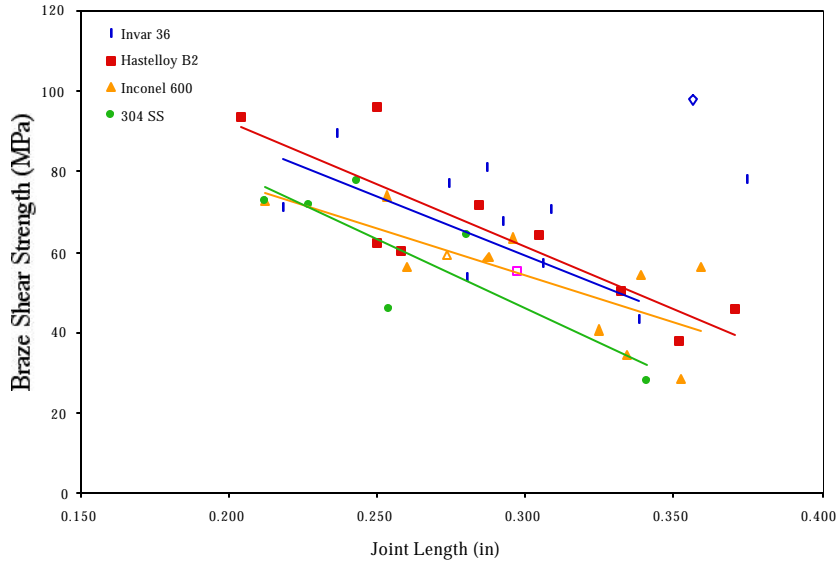
6

Figure 7: Load supported by concentric metal-ceramic joints. 3.5 mil braze thickness.

The FE model as a predictive tool

Ideally, we will be able to use the strain energy data generated by the FE models to predict the shear strength of a metal–ceramic joint, regardless of the base metal used. Thus, we need to compare the data from the models and experiments. Figure 8 shows how the experimental data correlates to the models.
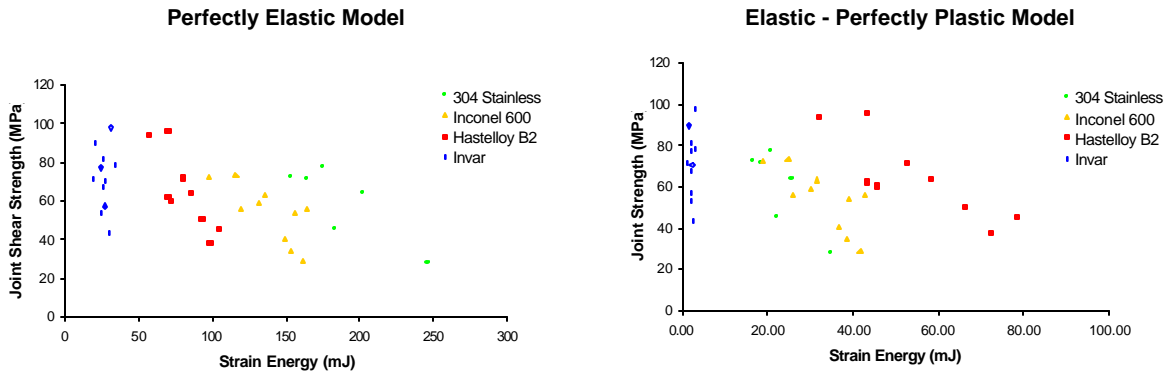

Figure 8: Correlation between elastic strain energy predictions and experimental data

For any material, the experimental joint shear strength is observed to decrease with increasing joint strain energy. However, the curves for the different materials do not coincide, which means that these models (metal behaving perfectly elastic or elastic-perfectly plastic) are not adequate to

describe residual stresses in the joints. However, the behavior of the base metal is probably strain-hardening.

A simulated strain-hardening model was developed, that assumed the work hardening line was 25% of the elastic stress value and 75% the plastic stress value for any given strain. Figure 9 shows the simulated stress-strain curve for Inconel 600 at room temperature.
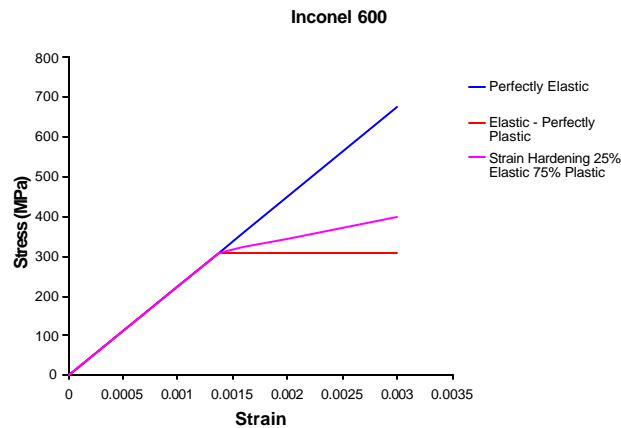

Figure 9: Simulated strain-hardening stress strain curve for Inconel 600 at room temperature.

Using the strain hardening model, three of the strain energy – joint shear strength curves to coincide (Figure 10).
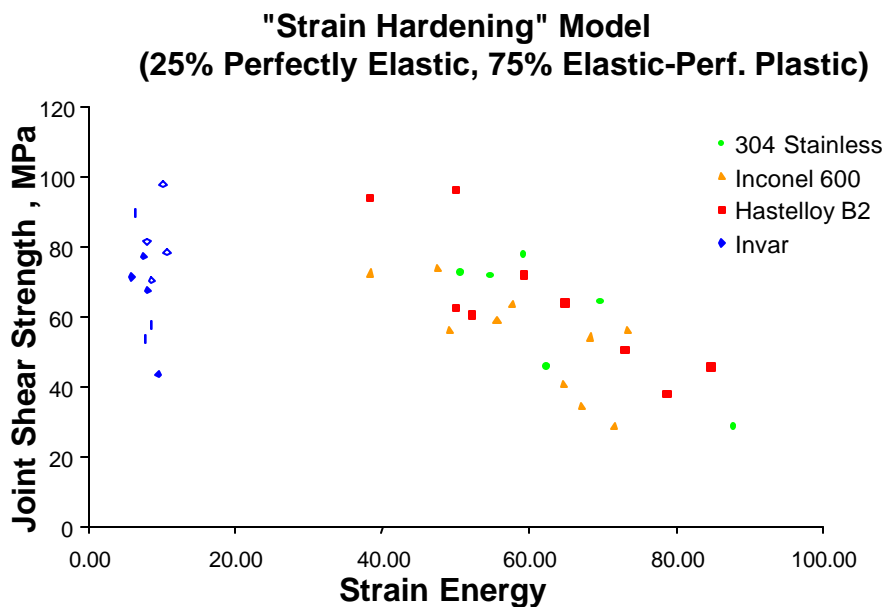

Figure 10: Strain hardening model

8

The curve representing invar-alumina joints does not coincide with the other curves because the calculated strain energy is much lower than that of joints made from the other, higher expansion materials. The low strain energy of the invar-alumina joints may explain why a subset of those joints exhibited such high strength and failed in the ceramic. However, it does not explain why most of the invar – alumina joints were not noticeably stronger than joints made with other materials.

In summary, the work to date has begun to elucidate what influences the mechanical behavior of ceramic-metal joints:
- The residual stresses resulting from CTE mismatch clearly degrade the strength of the joints.
- The majority of joints failed ductilly at the braze interface
- For this joint geometry, a peak load was supported when the joint was 0.25" long, and absolute strength decreased with joint length. Joint shear strength also decreases with joint length.
- Both the CTE mismatch and yield strength of the base metal appear to influence joint strength.
- The use of FE models to predict ideal joint strength is promising.

Future Work
There are still a number of tasks that need to be completed before we can develop design rules for metal-ceramic joints.

1. The effect of thermal cycling on joint strength will to be investigated. Joints will be subjected to 1 and 5 thermal cycles between 100C and 700C.
2. The FE model as a predictive tool will be refined. Use of different strain energy metrics, such as braze elastic strain energy, will be explored.
3. The anomalous behavior of the invar-alumina joints will be investigated.

TASK 3: Determine material mechanical properties under

conditions of high temperature and reactive atmosphere

Prof. Sukumar Bandopadhyay & Dr. Nagendra Nagabhushana
University of Alaska, Fairbanks

ABSTRACT

In the fifth quarter, initial experiments on the mechanical strength of La-Sr-Fe-O ceramic tubes in reducing conditions are reported. Tubes of Cr_2O_3 doped $LaSrFeO_3$ (20573 (a-f) were supplied by BP for strength characterization. The tubes were tested at 1000°C in Nitrogen environment. The results indicate that tubes showed a decrease in strength but with equivalent or a slight increase in Weibull modulus from as tested samples at room temperature. A distinctive change in fracture morphology was also observed.

Experimental procedure :

Sample Selection:

An important feature in the present set of experiments has been in choosing a well defined sampling procedure. Choosing representative samples for testing from a set of six tubes is important to collect pertinent information on several aspects such as:

1) The location of the test sample (viz. at near the center or at the edges of tubes)
2) Variation of processing flaws from near the center to the edge of the tube
3) Variations in strength from near the center to the edge of the tube.

For the present study, all the six tubes were rough-cut at their center and rings of length 9.5 mm were sliced from them. The rings were sorted evenly and two samples were randomly chosen. The specimens were then ground, polished and notched for regular C-ring tests. The present sampling method had a good control over the sample history and on the artifacts of specimen geometry.
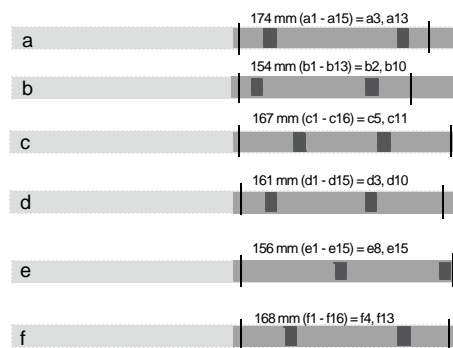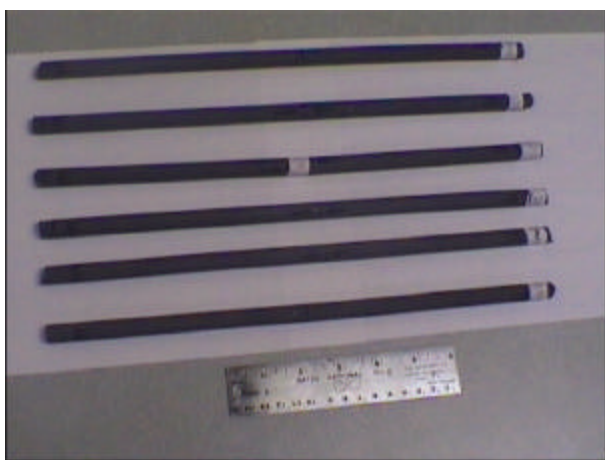
Fig. 1   Perovskite tubes (20572-53) and schematic of the test-sample history.

The specimens chosen for testing indicated variation in wall thickness. Variation was observed to be severe at the center as compared to at the edges and in some specimens ovality was observed in some of the samples. The variation in wall thickness is plotted as a function of the outer diameter of the tube and is as shown in figure 2.
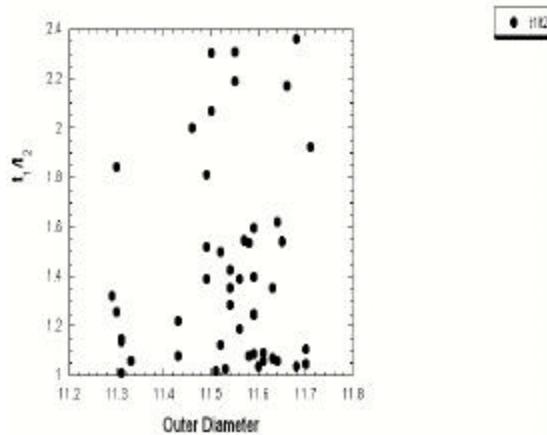

Fig. 2   Variation in the ratio of wall thickness to the outer diameter of the tube.

Testing

The C-ring specimen were tested in Ultra high purity Nitrogen flowing at a rate 10 l/min. A positive chamber pressure of 25PSI (0.17 MPa) was maintained through out the test. Stabilized Zirconia pressure pads were placed over the rings to avoid slippage of the rings during testing. The test temperature was raised to 1000°C and with a soaking period 15 mins. The specimens were loaded to fracture by loading in displacement control at a constant cross head speed 0.05mm/min.

Results

The results of the tests at high temperature are as shown in Table 1. The strength of the tubes decreased with temperature and pressure. A high of 226 MPa was observed which is nearly half of the maximum strength (429.1 MPa) observed at room temperature.

	20573 -53
Minimum Stress, MPa	96.5
Maximum Stress, MPa	226.7
Mean Stress, MPa	162.9
No. of Samples	12

Table 1:   Strength of the perovskite tubes at 1000°C and 0.17 MPa N_2

11

Fracture:

The specimens during the tests failed by shattering similar to as observed at room temperature. Fracture in the specimens were predominantly by cleavage. Microscopic analysis indicated strength distribution o be due to both surface and volume flaws. However, fracture was seemingly controlled by volume relate process flaws. Interestingly, there seemed to be a good relief between the particle boundary and the particles Also failure mechanisms such as pores at grain-boundary triple points and grain-boundary cavitations typical of temperature assisted failure were observed.
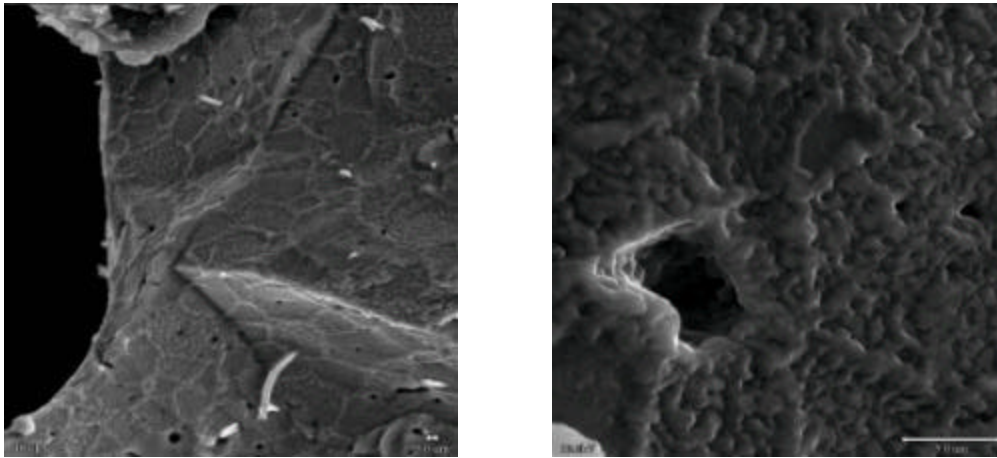
Fig. 3   Fracture initiation flaws – a) Surface and b) volume.

Weibull Analysis

The results of strength distribution was platted in a two – parameter Weibull plot as shown in Fig 4.
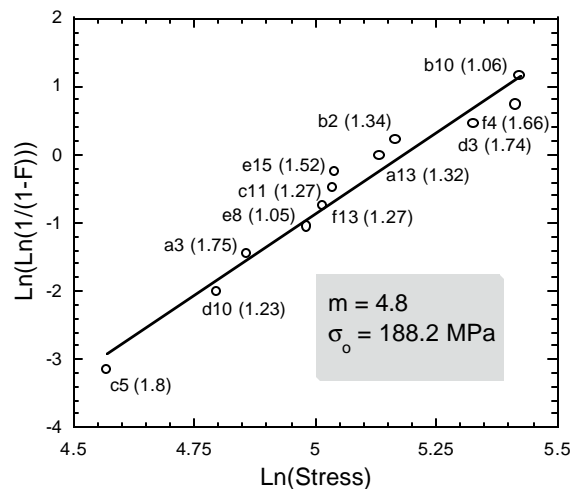

Fig.4   Weibull plot for samples tested at 1000°C and 0.17 MPa N_2

Weibull analysis indicated the Weibull parameter (m) to be 4.8, which was a slight increase from at the room temperature value of 4. The analysis also indicated no significant effect of the specimen history on the strength distribution.

Conclusion and Future work

Although the strength of the tubes decreased with temperature a complementary increase in Weibull modulus was observed. The increase in the parameter `m' could possibly be attributed to the various surface reactions and blunting of surface flaws. However, the increase was not significantly high and the modulus values would probably converge to the same values with larger number of samples tested.

Further work is necessitated to correlate the microstructural aspects to strength and fracture in the perovskite tubes. Also, it is important to generate Weibull plot in different atmospheres to study the effect of surface reaction on the strength.

Task 4: Preparation and characterization of Dense Ceramic Oxygen Permeable Membrane

Dr. Harlan U. Anderson, Director of EMARC
Dr. Wayne Huebner, Dr. Yixiang Xie
University of Missouri- Rolla

Summary

Two compositions of mixed-cation oxide powder, $La_{0.60}Sr_{0.40}Fe_{0.85}Ga_{0.15}O_3$ (A) and $La_{0.20}Sr_{0.80}GaO_3$ (B) were prepared by a modified Pechini liquid mixing method [1, 2]. While X-ray diffraction patterns taking on (A) composition show a major Perovskite phase, composition (B) exists as an mixture of La, Sr, and Ga oxides. Neutron diffraction measurement indicates that $(La_{0.59}Sr_{0.40})_{0.99}Fe_{1.0}O_3$ has a rhombohedral structure at 1000 °C under air condition and under a reducing atmosphere. Peak broadening is evidence of starting phase separation under a strong reducing atmosphere (1000 °C, 90% CO/10% CO_2, log Po_2 = -16.1), a confirmation that previous TGA and thermal expansion measurement also suggest the phase stability with logPO2 higher than –16.1. The conductivity of $(La_{0.59}Sr_{0.40})_{0.99}Fe_{1.0}O_3$ shows a p-n transition with decreasing PO2. Archimedes density measurement [3 – 6] gives its sintered densities to be 3.61-5.95 g/cm^3 depending on sintering temperature 800 – 1200 °C, which are 60.0 – 99.3% its theoretical density of 5.99 g/cm^3.

Experimental

$La_{0.60}Sr_{0.40}Fe_{0.85}Ga_{0.15}O_3$ (A) and $La_{0.20}Sr_{0.80}GaO_3$ (B) were prepared through the same process described in report 1 but at a 800 °C calcination temperature. Disk (sintered at 1200 °C, isostatic press at 45,000 psi) x-ray diffraction measurements were carried out on a SINTAG 2000 x-ray diffractometer. Neutron Diffraction Measurements were done at the Reactor of University of Missouri-Columbia. Disk samples for Neutron Diffraction measurements (wavelength: 1.4875 Å)

were reheated at 1000 °C under air, 10% CO/90% CO_2, 50% CO/50% CO_2, and 90% CO/10% CO_2, respectively for 24 hours and quenched under the respect atmospheres. Liquid displacement technique [3-6] was used to measure the densities of the sintered discs. A Sartorius scale was employed. The standard density kerosene used is 0.787 g/cm^3. Thermal expansion experiments were done by a modified Orton 1600 dilatometer. The weight losses in different atmosphere were measured using a CAHN TG171. Absolute oxygen content was determined by redox titration of a quenched powder sample from 1000 °C to room temperature in air. Electrical conductivity of a bar was measured using a SI 1286 Electrical Interface (Solartron).

Sintering Process of $(La_{0.59}Sr_{0.40})_{0.99}FeO_3$

Step	Ramp, minute	Temperature, °C	Dwell, minute
1	300	100	300
2	300	200	300
3	300	300	300
4	300	400	300
6	800	800	300
7	50	1200	600
8	60	800	-
9	600	room	-

Quenching process of $(La_{0.59}Sr_{0.40})_{0.99}Fe_{1.0}O_3$ discs for neutron Diffraction

Atmosphere	Ramp, minute	Temperature, °C	Dwell, hour	Quench to, °C
Air	200	1000	24	25
10% CO/90% CO_2	200	1000	24	25
50% CO/50% CO_2	200	1000	24	25
90% CO/10% CO_2	200	1000	24	25

Results and Discussion

Figure 1, and 2 show the XRD patterns of disk $La_{0.60}Sr_{0.40}Fe_{0.85}Ga_{0.15}O_3$ (A) and $La_{0.20}Sr_{0.80}GaO_3$ (B), which indicate major Perovskite phase for (A) and multi-phase of La, Sr, and Ga oxides for (B). Like Zr, and Ce, ionic radius of Ga is rather bigger than that of Fe. Previous research indicated that Zr and Ce doping created phase instability of a Perovskite structure. Composition (B) was made twice and XRD proved it a multi-phase composition. Total substitution of Ga for Fe is not recommended.
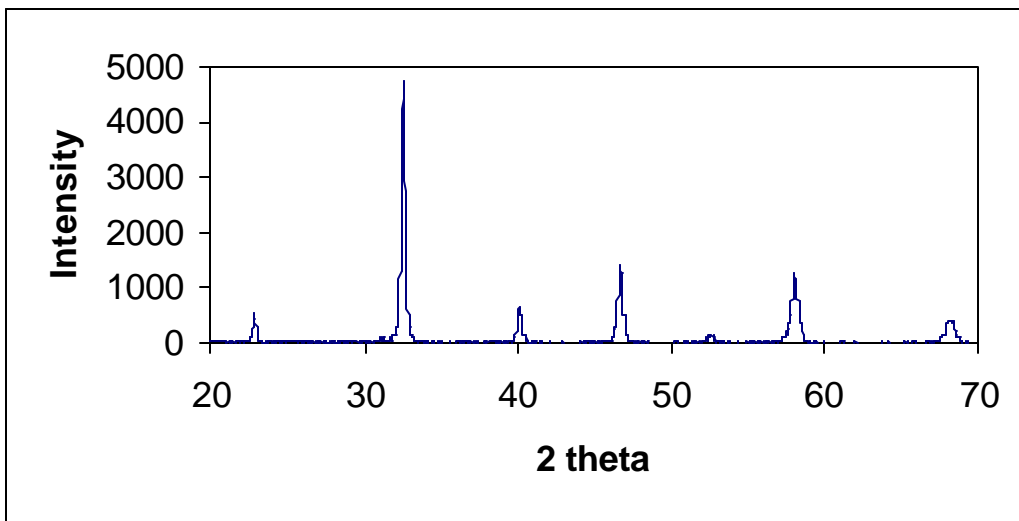
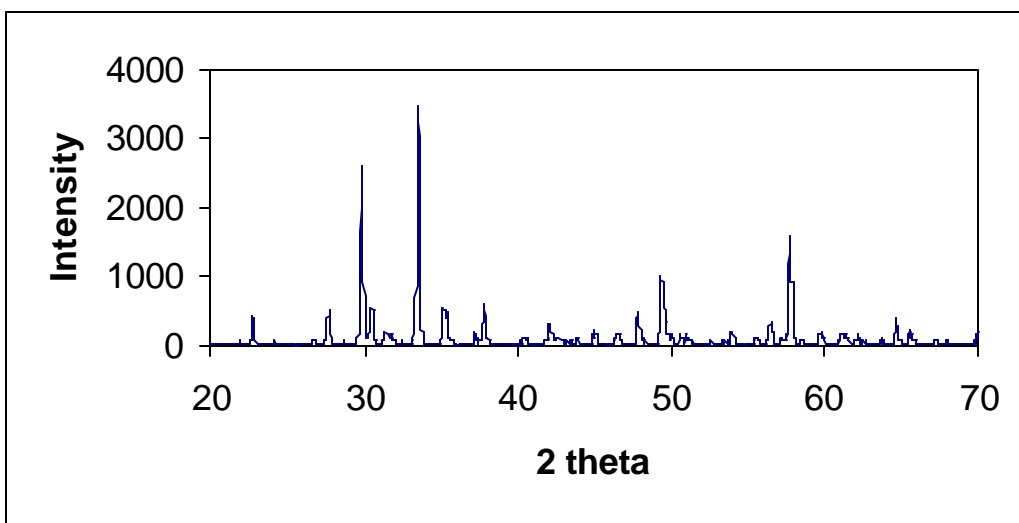Figure 1. XRD pattern of disk $La_{0.60}Sr_{0.40}Fe_{0.85}Ga_{0.15}O_3$ (A), a major Perovskite phase

Figure 2. XRD pattern of disk $La_{0.20}Sr_{0.80}GaO_3$ (B), a multi-phase of oxides

Repeated TGA measurement and titration of $(La_{0.59}Sr_{0.40})_{0.99}FeO_{3-\delta}$ determines the oxygen content under different atmospheres at 1000 °C in this material, which is shown in Table 1. The oxygen content difference in this material under Air and 10% CO/90% CO_2 is 0.16 that is big enough to generate the phase transition indicated by ND patterns. Its difference, 0.02, under 10% CO/90% CO_2 and 10% CO/90% CO_2 is small, and respectively there is no significant peak intensity change observed in those two ND patterns. When oxygen loss from stoichiometry reaches 12% under 90% CO/10% CO_2 at 1000 °C (log PO_2), the composition starts decomposition as XRD and ND data suggested.

Table 1. Equilibrium oxygen content in $(La_{0.59}Sr_{0.40})_{0.99}FeO_{3-\delta}$ at 1000 °C

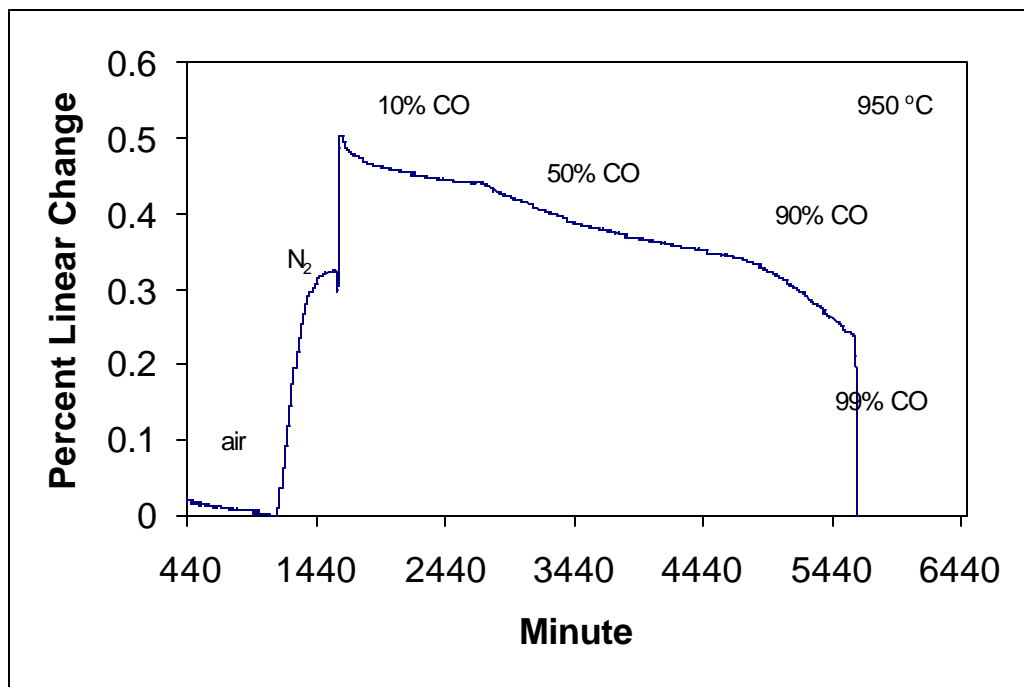| Atmosphere	3-δ
Air	2.88
N_2	2.82
1% CO/99% CO_2	2.74
10% CO/90% CO_2	2.72
50% CO/50% CO_2	2.70
90% CO/10% CO_2	2.64
99% CO/1% CO_2	2.13* not equilibrium

Figure 3. Thermal Expansion of dense $(La_{0.59}Sr_{0.40})_{0.99}FeO_3$

Figure 3 shows thermal expansion of dense $(La_{0.59}Sr_{0.40})_{0.99}FeO_3$, at 950 °C. Equilibrium data of thermal expansion relative to the sample under air condition is listed in Table 2.

Table 2. Thermal Expansion at 950 °C of $(La_{0.59}Sr_{0.40})_{0.99}FeO_3$

Atmosphere (log PO_2)	Linear Change %
Air (-0.68)	0
N_2 (--5)	0.32
10% CO (-13.2)	0.44
50% CO (-15)	0.36
90% CO (-17)	0.24
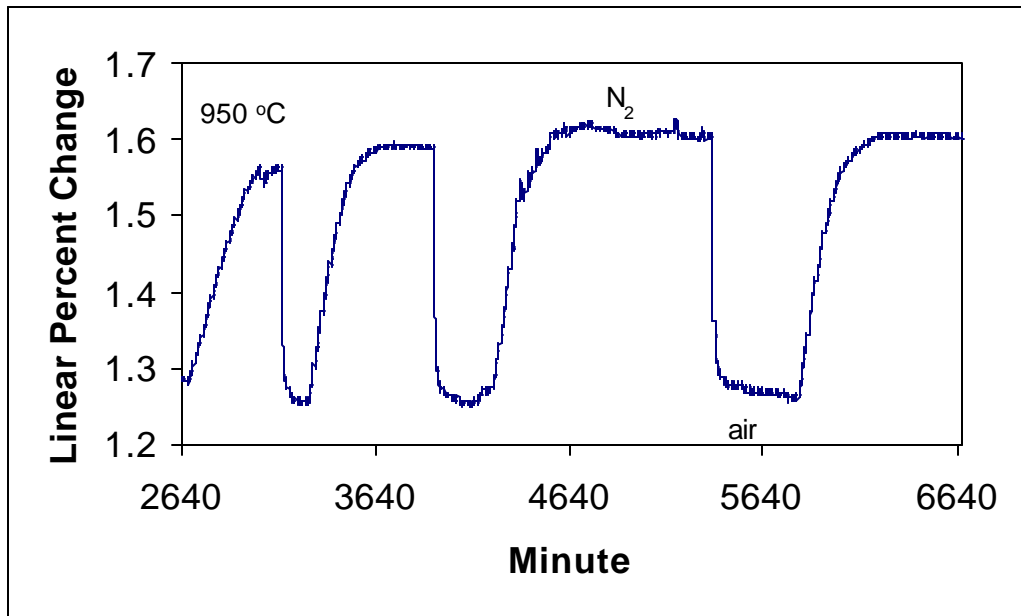
Figure 4. Thermal Expansion of dense $(La_{0.59}Sr_{0.40})_{0.99}FeO_3$

Figure 3 shows reversible thermal expansion of dense $(La_{0.59}Sr_{0.40})_{0.99}FeO_3$, at 950 °C under air-$N_2$ circulation.

Remeasurement of electrical conductivity of $(La_{0.59}Sr_{0.40})_{0.99}FeO_3$ led to agreement with previous results.

Archimedes density measurement [3 – 6] gives its sintered densities (Table 3) of $(La_{0.59}Sr_{0.40})_{0.99}FeO_3$ to be 3.61-5.95 g/cm^3 depending on sintering temperature 800 – 1200 °C, which are 60.0 – 99.3% its theoretical density of 5.99 g/cm^3. To reach a dense material for this composition, a sintering temperature will have to be at least 1200 °C.

Table 3.

Sintering temperature, °C	Bulk density, g/cm^3
800	3.61
900	4.01
1000	5.14
1100	5.83
1200	5.94

Composite Structures

In order to put dense films on porous support substrates it is necessary to reduce the diameters at the surfaces and to make the surfaces smoother. Studies have been initiated to achieve these goals.

The initial studies were done using colloidal ceria as the surface treatment layer.

Nanocrystalline cerium oxide powder with an initial grain size of approximately 5nm was produced using an aqueous precipitation processing route. 99.999% cerium (III) nitrate (Alfa Aesar, Inc.) was dissolved in distilled water and precipitated to cerium hydroxide particles using hydrogen peroxide and ammonium hydroxide.

Aqueous colloidal suspensions were prepared by mixing 10 weight percent of CeO_2 powder in pH 4 distilled water (balanced with HNO3) along with 5 weight percent butoxyethanol to aid in drying and decrease the wetting angle. The butoxyethanol also partially polymerizes due to the acidic content of the solution, and as a consequence aids in increasing the solution viscosity and in the formation of a continuous film. The power was then dispersed in the solution using a high intensity ultrasonic probe for about one hour. The solution was then filtered through a 0.45μm glass fiber filter (Whatman, Inc.) in order to remove any foreign matter.

Thin films of CeO_2 were prepared by spin coating the colloidal suspension on a variety of substrates. Optical quality, both sides polished (0001) oriented sapphires substrates were used for both the optical measurements as well as the DC conductivity measurements.

Films were spun on the prepared substrates at 1500rpm for 30 seconds and subsequently dried at 70°C for about an hour. The films were then heat treated at 350°C for about an hour and

cooled back to room temperature after which subsequent coatings could be deposited. Sintering of the porous films was done in a standard furnace using a ramp rate of 5°C/min to the maximum temperature, at which they were held for 2 hours.

The sintered films were characterized according to their grain size, thickness and density using X-ray diffraction, mechanical profilometry, ellipsometry, and UV-Vis spectroscopy, as shown in previous studies. The results as to the grain size, film density and thickness are shown in figures 5-10. Initially, the films have a density of approximately 50% and a grain size of 5nm after 400°C and densify to 85% with a grain size of 60nm after annealing at 1000°C. The X-ray diffraction patterns of CeO_2 samples on sapphire substrates annealed at different temperatures showed that the films are single-phase fluorite structured and show no reaction with the substrate over the investigated temperatures. Peak broadening grain size calculations (Reitfeld analyses) from the diffraction patterns correlate well with those in FESEM images (figure 8).
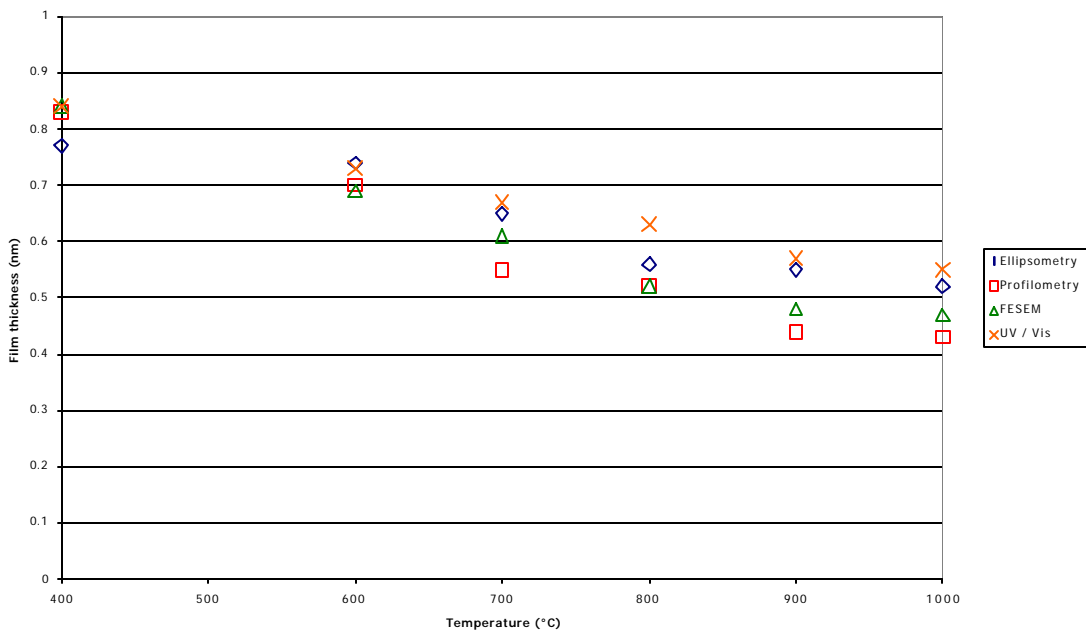

Figure 5. Variation in the film thickness of porous CeO_2 thin films as a function of annealing temperature as measured with different techniques.
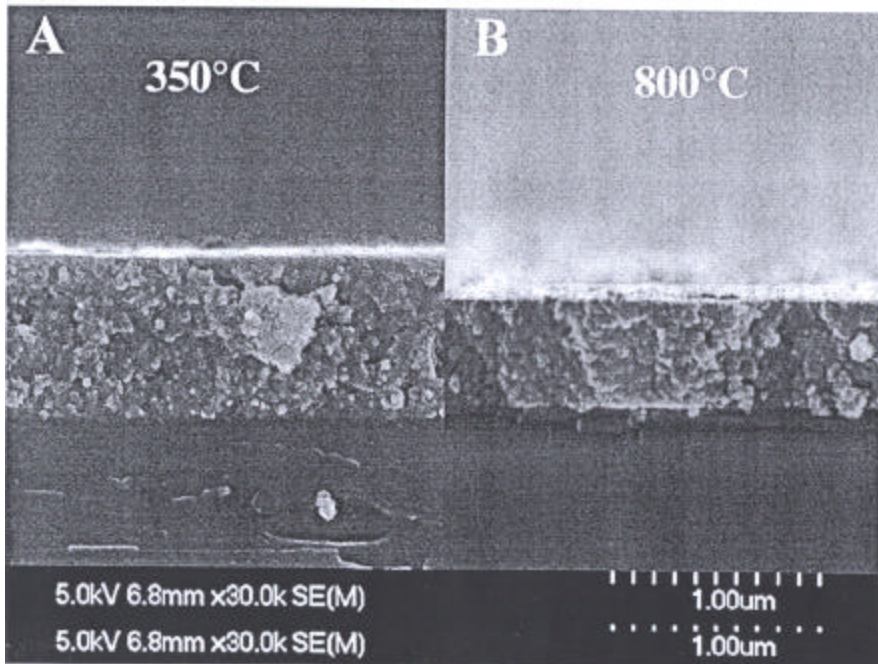
Figure 6. SEM cross-sections of CeO$_2$ coatings on the sapphire substrate. A, B – after sintering at 400°C and 800°C correspondingly.
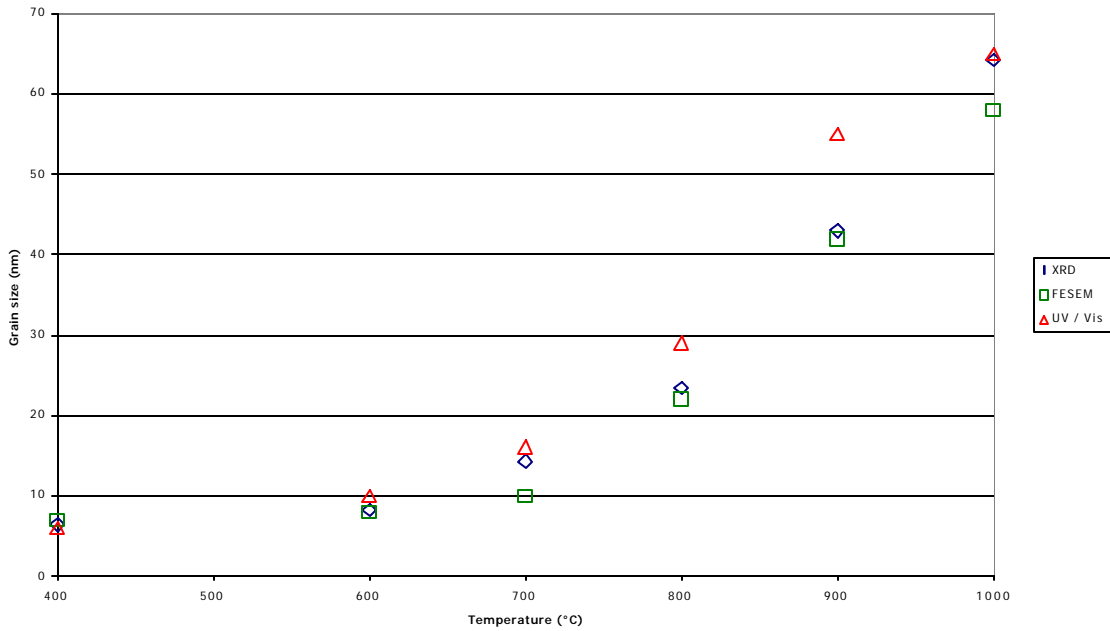

Figure 7.
Variation in the grain size of porous CeO$_2$ thin films as a function of annealing temperature as measured with different techniques.
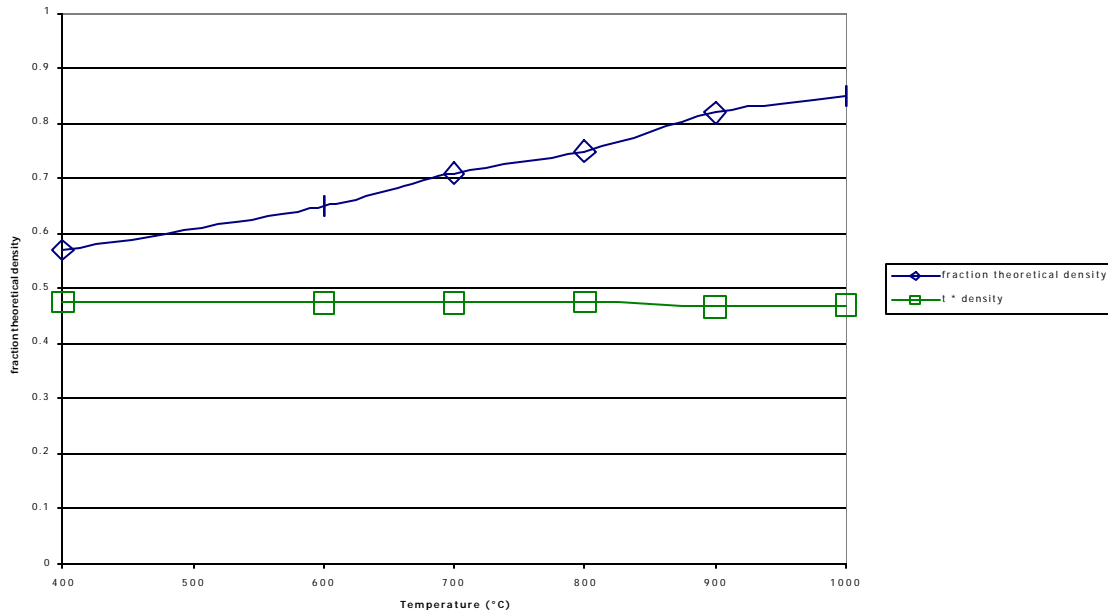
Figure 8.   Variation in the density of porous CeO$_2$ thin films measured with UV/Vis spectrophotometry as a function of annealing temperature.
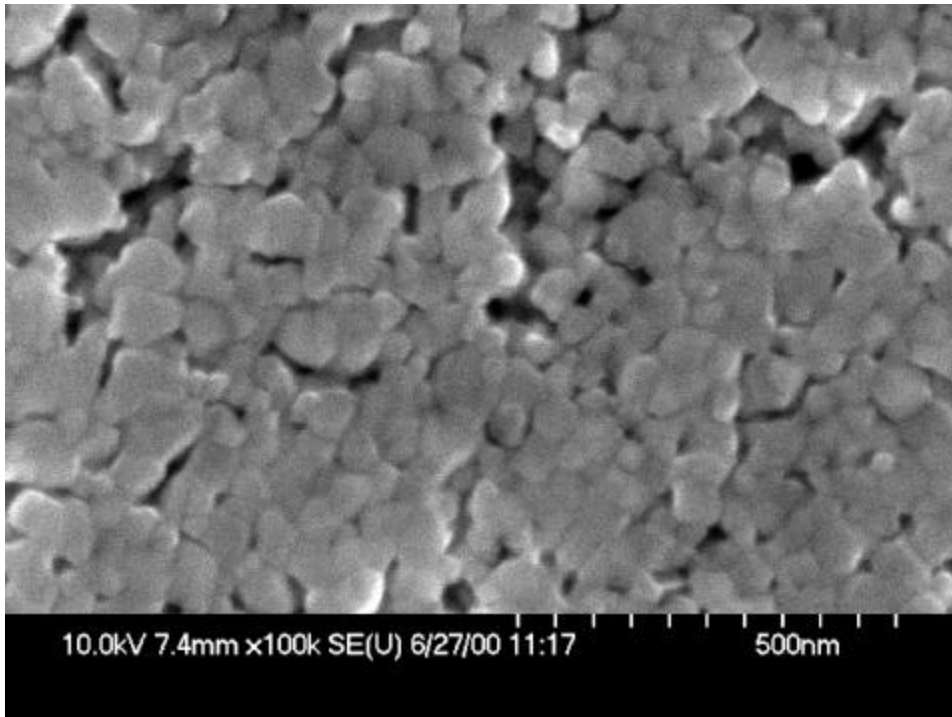

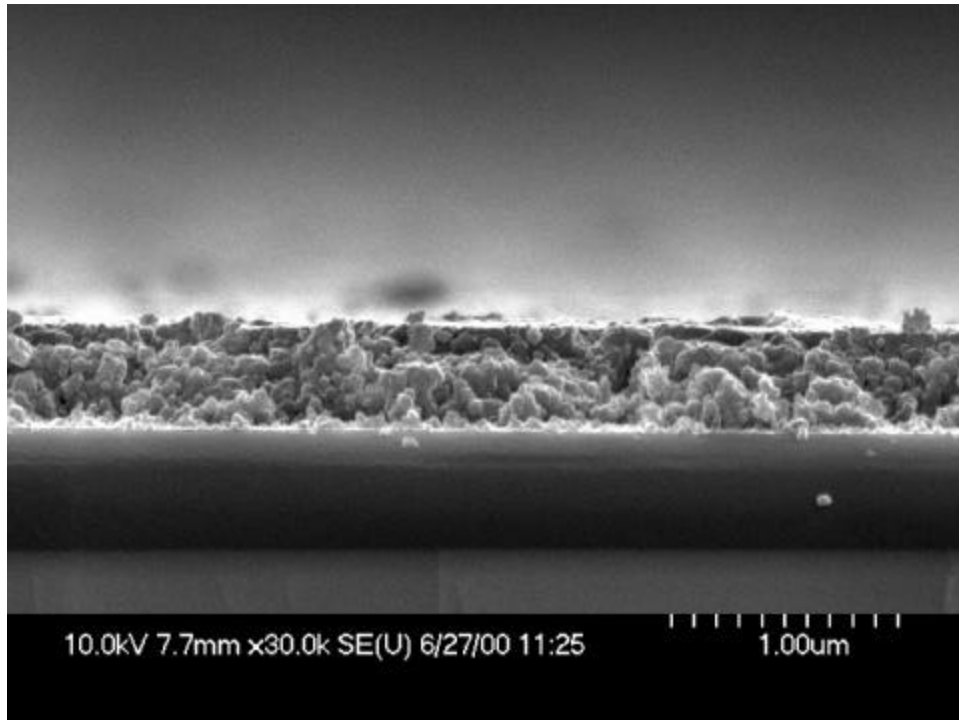Figure 9. Surface of Ceria film on sapphire which was sintered at 1000°C.

Figure 10. Cross-section of Ceria film on sapphire sintered at 1000°C.

After the initial experiments of depositing ceria onto sapphire had established the deposition process, experiments were started in which the colloidal ceria was deposited onto a porous $(La,Sr)MnO_3$ (LSM) substrate. Figures 11 & 12 show some of the deposition. Figure 13 shows that a dense zirconia film can be formed on the ceria coating.

The important lessons that have been learned are:

1) To be able to form a dense film from polymer precursor solutions on porous substrate, the surface must not have pores that are larger than about 0.2μm.
2) Colloidal ceria can form a smooth surface on a very porous (>10μm diameter pores) surface onto which polymer precursor techniques can be used to produce dense (<1μm thick) films.
3) The thickness of ceria film must be in the order of the roughness of the underlying substrate before dense films can be formed.
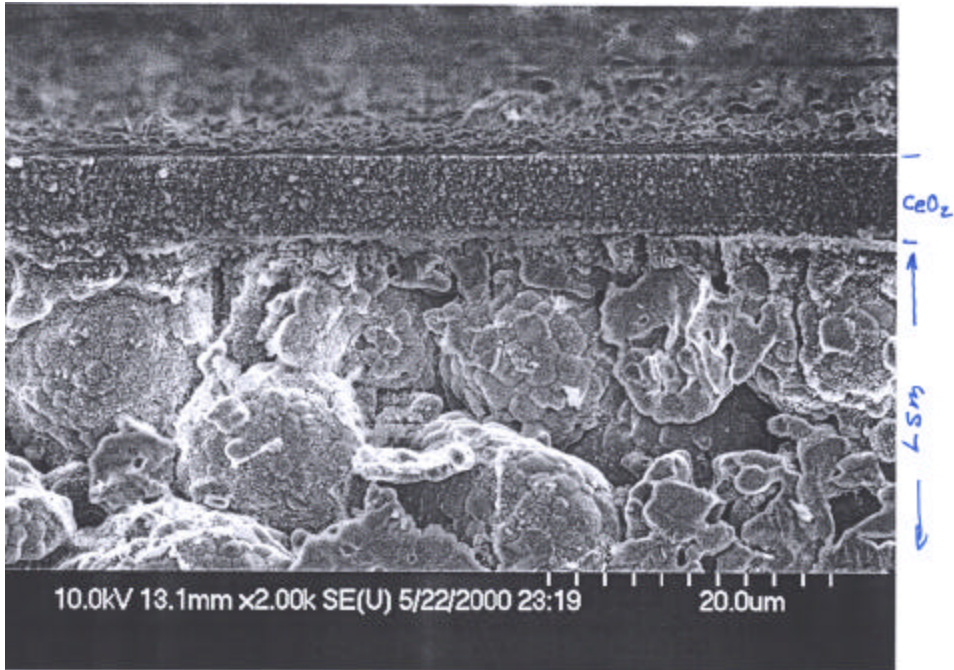
Figure 11. Colloidal CeO$_2$ porous (60%) th. Density) thin film on porous LSM substrate. Composite was sintered at 1000°C.
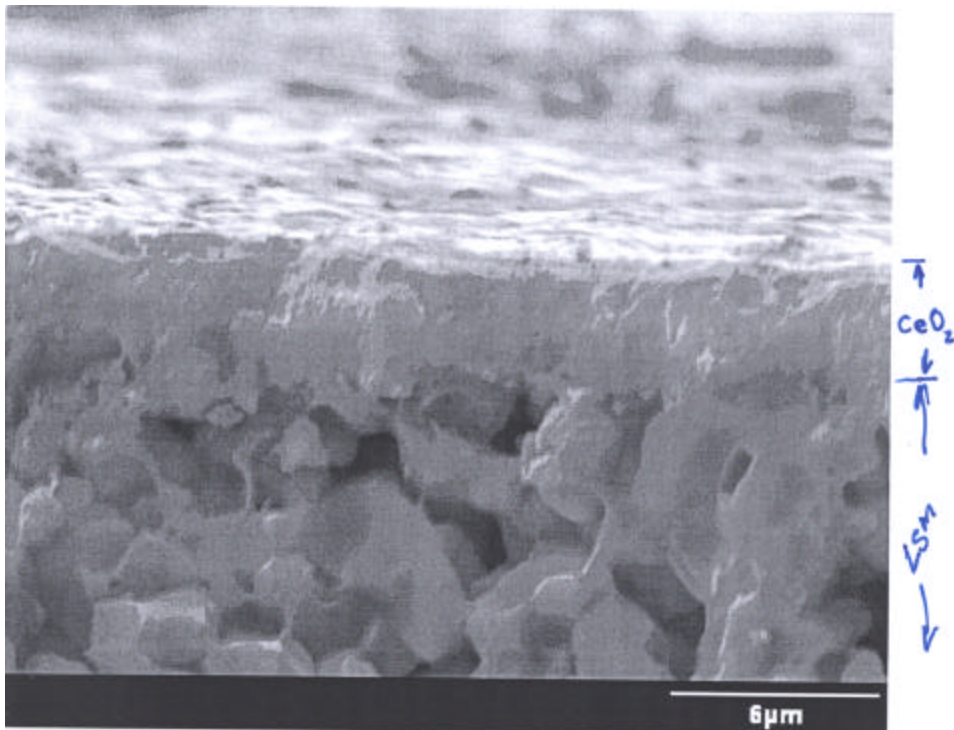
Figure 12. Colloidal ceria planarizing layer. Cross section, high resolution. Sintering temperature of composite = 1000°C.
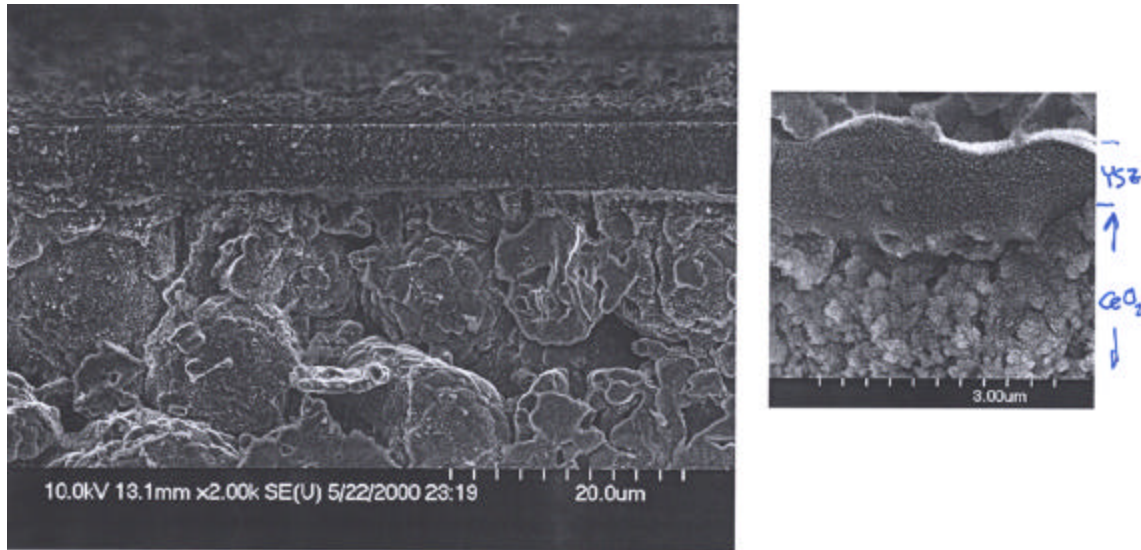

Figure 13. Field-emission SEM micrograph of a YSZ/Colloidal CeO_2/spray-pyrolized LSM composite. CeO_2 = 5µm, YSZ = 0.5µm. Composite sintered at 800°C.

Neutron Diffraction

<div align="center">

Report on preliminary studies of $La_{0.6}Sr_{0.4}FeO_{3-d}$
W. Yelon and Z. Chu

</div>

Four samples of the title compound, which had been subject to different heat treatments, were studied using neutron diffraction at the University of Missouri research reactor and the data analyzed using the FULLPROF code for Rietveld analysis. A number of different models were tested based on the parent cubic perovskite structure. Because of the sensitivity of neutron diffraction to the magnetic ordering of the Fe atoms, it was necessary to simultaneously model the magnetic ordering and the nuclear structure. However, the change in magnetic order observed between the air quenched sample and that seen in the reduced samples provided some insight into the physics of these materials.

None of the data sets showed evidence for anything other than single phase materials, except that the 90% CO/10% CO_2 reduced sample is beginning to show peak broadening and asymmetry, suggesting the possibility of incipient decomposition of the sample.

Four models were found to give "reasonable" fits to the data, and each was tested for each sample. The statistical tests, however, show that the preferred model is different for the reduced samples than for the air quenched samples.

There are some notable differences between the neutron iffraction diagrams for the reduced samples and the other (Figures). The diffraction peaks for the reduced samples are significantly sarper than for the other. It was initially assumed that this represented a change to a higher symmetry group with fewer reflection, but no satisfactory fits could be achieved with cubic groups, and the rhombohedral models are the highest symmetry that can satisfactorily fit any (and all) of the data sets. The first diffraction peak (at about 19°) is much stronger in the reduced samples than in the air quenched samples. This peak proves to be purely magnetic and the change reflects a large increase in magnetic moment for the reduced samples vs the air quenched samples.

The Models

Model 1: The first model was found to apply to the air quenched sample. It is a pure rhombohedral (R-3C) space group with unit cell volume around 360 D^3 for the tripled hexagonal setting of the cell, i.e. six times the volume of the basic cubic perovskite cell. In this model there is only one oxygen site at the position 0.54 0 0.25. Within this model the magnetic scattering was modeled as antiferromagnetic with moments along the hexagonal c-axis, which reverse between the positions 0 0 0 and 0 0 ½. The magnetic model has the symmetry R-3.

Model 2: refinement of the reduced samples using model 1 left significant residuals in the difference between observed and calculated intensities. Fourier mapping showed that oxygen atoms appeared to (partially occupy additional positions. Model 2 introduces a second oxygen position (approximate coordinates 0.26, 0.39, 0.07). The occupation of both the normal position and this additional position were allowed to vary. The magnetic model is the same as employed for model 1.

Model 3: The refinements in model 2 show significant occupation of both the oxygen sites, with a relatively small distance between them. Model 3 examines the possibility that the correct model has only a single oxygen site somewhere between the sites found by model 2. In principle Model 2 should show this directly, by reducing the occupation of the "ideal" octahedral site to zero while filling the second site to the net oxygen occupancy. However, it is not always possible to arrive at such a solution from the starting point for model 2 and thus model 3 is examined separately. The magnetic model is the same as employed for model 1. It is interesting to note that the position for the oxygen refined in this model is significantly different for the reduced samples than for the other one.

Model 4: We decided to test if the symmetry might be lower than rhombohedral by using an orthorhombic space group with dimensions $a^2 \times a^2 \times 2a$, with respect to the fundamental cubic perovskite cell. This cell contains 4 formula units (240 D^3) compared to the six formula units in the hexagonal representation of the rhombohedral cell. In this space group there are naturally 2 different oxygen sites, with full occupancies of 4 and 8 respectively. The magnetic structure is modeled in P-1 symmetry, but is essentially the same as in the rhombohedral models.

Results

Table 3 shows some of the results of refinement using these four models. The unit cell volumes (using the R-3C results). The unit cell volumes (using the R-3C results) of the three reduced samples differ by about 0.15%, while they differ from that of air quenched sample by about 5 D^3. The c/a ratio changes from 2.432 for the air quenched sample to 2.448 for the reduced samples. This change affects the peak positions and the apprent sharpness of the diffraction peaks.

The good ness-of-fit measure X^2 for model 4 is distinctly worse than the best result and this model is discarded. For the air quenched sample model 3 gives a slightly better result than model 1, suggesting that the oxygen atoms are slightly displaced from the "ideal" positions. The difference, however, is slight and might not be significant. All four models show that the oxygen concentration is 3 to within the experimental error of about 0.03. The two-site model fails for these cases.

For the three reduced samples the lowest X^2 is observed for the two site model (model 2). In this case the calculated vacancy concentration increases from 7.2% to 7.8% to 8.8% for the 10% CO, 50% CO and 90% CO samples respectively. It is possible that the octahedra containing oxygen vacancies are distorted from the "ideal" position, while those are fully occupied are close to ideal. It is very likely that correlated motion of adjacent octahedra is actually produced, but further modeling would be necessary to describe this in detail.

The magnetic models for the all five samples are the same, antiferromagnetic Fe coupling the Fe at 0 0 0 with that at 0 0 ½ by a 180°rotation from up to down. However, the Fe moments for the three reduced samples refine between 3.72 and 3.82 μ_B while the moments for the other is much more smaller ($1.4\mu_B$) for the air quenched sample.

Table 3. $La_{0.6}Sr_{0.4}FeO_{3-d}$

Sample	1000°C air quenched	1000°C-10%CO/90% CO$_2$	1000°C-50%CO/50% CO$_2$	1000°C-90%CO/10% CO$_2$
Model 1				
chi**2	3.31	16.1	11.6	14.9
% vac	0	6.8	8.1	9.6
Fe moment	1.41	3.81	3.84	3.75
a	5.527	5.54	5.542	5.547
c	13.441	13.56	13.564	13.582
vol	355.6	360.41	360.84	361.96
Model 2				
chi**2	4.3	8.97	6.6	10.8
% vac	0	7.2	7.8	8.8
Fe moment	1.43	3.82	3.82	3.72
a	5.527	5.54	5.542	5.547

c	13.441	13.56	13.564	13.582
vol	355.6	360.41	360.84	361.96
Model 3				
chi**2	3.1	9.7	7.06	11.1
% vac	0	7.23	8.41	8.14
Fe moment	1.42	3.86	3.88	3.77
a	5.527	5.54	5.542	5.547
c	13.441	13.56	13.564	13.582
vol	355.6	360.41	360.84	361.96
Model 4				
chi**2	8.92	14.8	10.2	11.8
% vac	0	8.3	9.1	8.1
Fe moment	1.19	3.74	3.77	3.62
a	5.532	5.541	5.543	5.545
b	5.5	5.536	5.538	5.555
c	7.798	7.833	7.837	7.833
vol	237.28	240.26	240.54	241.31

Model 1 R-3C symmetry, ideal oxygen octahedral=Ov-refined oxygen concentration

Model 2 R-3C symmetry, partial ideal oxygen Or (x, 0, 0.25, x = 0.533) partial displaced oxygen
O5r (0.266, 0.384, 0.074)

Model 3 R-3C symmetry, displaced oxygen only O5s (0.3, 0.37, 0.06)

Model 4 Pbnm symmetry (two oxygen sites) oxygen occupancy refined
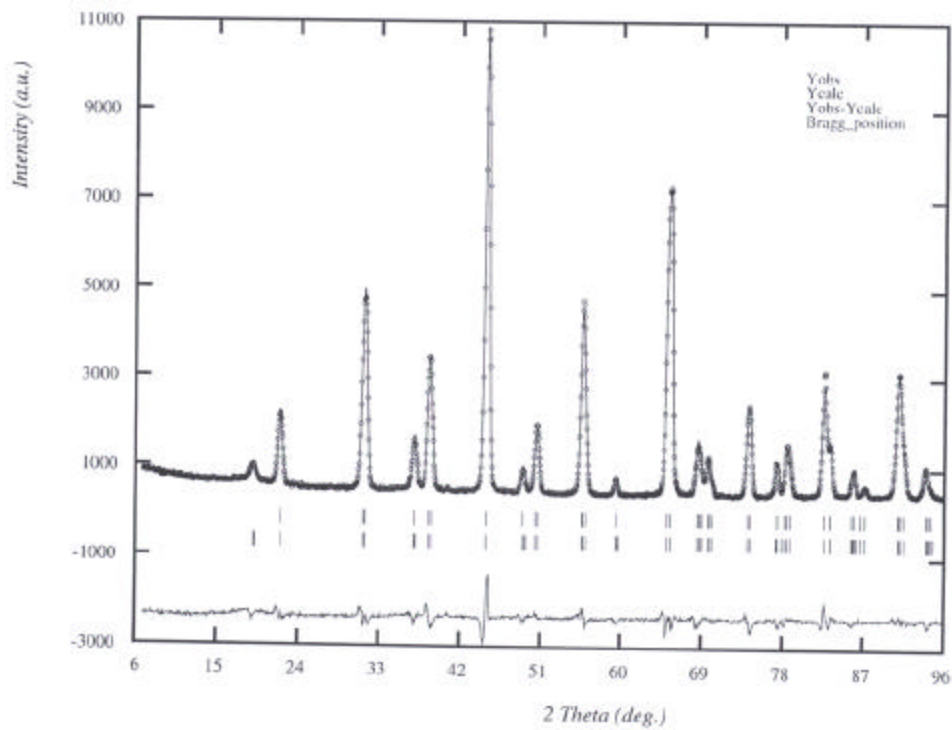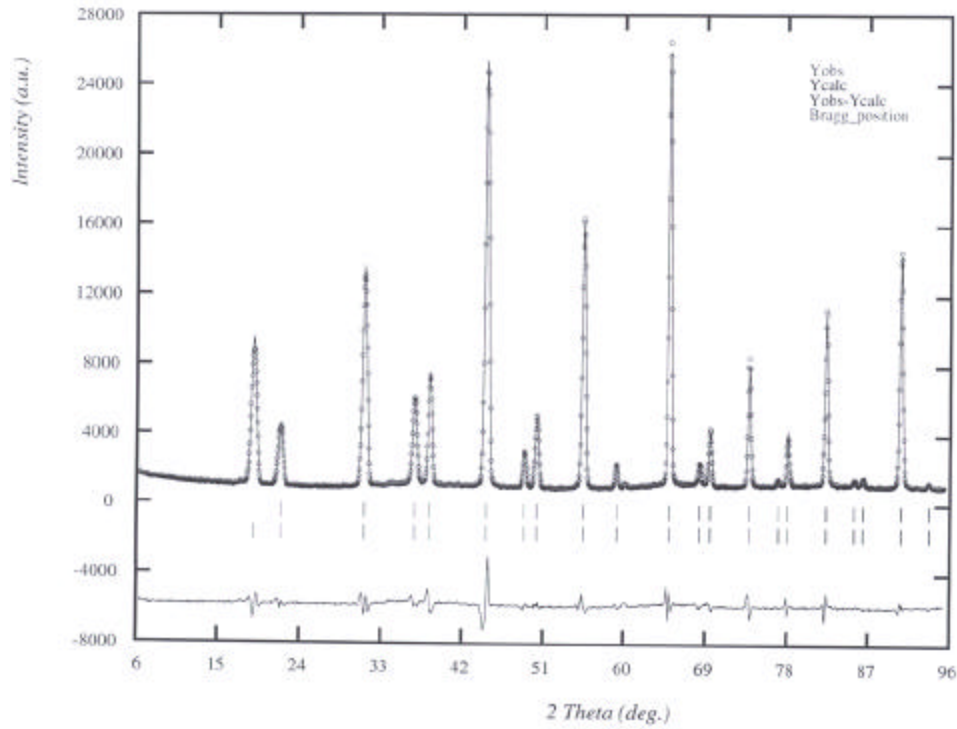
Figure 14. v258 R-3C+R-3mag PSC 1000 Air Quench

Figure 15. r261 R-3C+R-3mag SPC 1000C Quench 10%CO/90%CO$_2$

Conclusions

The air quenched sample is close to stoichiometric with less than 1% vacancies on the oxygen lattice. The best refinement has the oxygen atoms at, or very close to their ideal positions in rhombohedral setting of the perovskite cell. The magnetic moment of the Fe is small, around 1.4 μ_B.

The oxygen vacancy concentration increases from 7.2% to 8.8% as the reducing treatment changes from 10% CO to 90% CO. The last sample appears to show some sign of decompositin in peak broadening, but can still be refined as a single phase specimen. The estimated standard deviations on the refined vacancy concentration is about 4%. The monotonic change with oxygen partial pressure suggests that the errors may, in fact, be somewhat smaller. Nevertheless, the neutron diffraction should be a good gauge for the following trends.

These experiments are quite straightforward, requiring about 1 g samples and 4-12 hours of data collection depending on the statistical precision desired. Once models are established the refinements proceed rapidly and many models can be tried or data sets analyzed in a brief period.

- For $La_{0.20}Sr_{0.80}FeO_{3-\delta}$, replacing Fe with 35% Cr is not recommended due to $SrCrO_4$ formation.

- For $La_{0.59}Sr_{0.40}FeO_{3-\delta}$, replacing Fe with 15% Ti stabilizes the perovskite structure.

- XRD pattern of $(La_{0.60}Sr_{0.40})_{0.99}FeO_{3-\delta}$ of surface of sintered disk does not show evidence of second phase.

1. Neutron diffraction patterns of $(La_{0.60}Sr_{0.40})_{0.99}FeO_{3-\delta}$ powder show:
   - single phase rhombohedral structure (in air at 1000 °C, logPO2 = -0.7) and under 10% CO/90% CO_2 (logPO2 = -12.1) and 50% CO/50% CO_2 (logPO2 = -14.1).
   - decomposition starts under 90% CO/10% CO_2 at 1000 °C (logPO2 = –16.1).

- XRD pattern of sintered disk of $La_{0.60}Sr_{0.40}Fe_{0.85}Ga_{0.15}O_3$ shows nearly 100% perovskite phase.

- $La_{0.20}Sr_{0.80}GaO_3$ is multi-phase.

- Applying a stress on a disk introduces lattice parameter shifts and non-reversible deformation.

- > 98% theoretical density of $(La_{0.59}Sr_{0.40})_{0.99}FeO_3$ can be reached at a sintering temperature 1200 °C.

- Colloidal ceria can be used to act as a interface between large pore size substrates (>10µm) and dense films.

References

1. M. P. Pechini, "Method of Preparing Lead and Alkaline Earth Titanates and Niobates and Coating Method Using the Same to Form a Capacitor," U. S. Pat. No. 3,330,697, 1967.

2. N. G. Eror and H. U. Anderson, 'Polymeric Precursor Synthesis of Ceramic Materials"; pp571-77 in Better Ceramics through Chemistry II, Proceedings of Materials Research Society Symposium, Palo Alto, CA, April 1986. Edited by C. J. Brinker, D. E. Clark, and D. R. Ulrich. Materials Research Society, Pittsburgh, PA, 1986.

3. James Reed, Introduction to the Principles of Ceramic Processing, Chapter 8, pp118-133, John Wiley, New York 1994.

4. J. T. Jones and M. F. Berard, Ceramics: Industrial Processing and Testing, 2nd Edition, pp. 156-177, Iowa State University Press, Ames, Iowa 1993.

5. ASTM C 830-88, "Apparent Porosity, Liquid Absorption, Apparent Specific Gravity and Bulk Density of Refractory Shapes by Vacuum Pressure".

6. ASTM C 20-87, "Apparent Porosity, Water Absorption, Apparent Specific Gravity and Bulk Density of Refractory Brick and Shapes by Boiling Water".

Future

- Further thermal expansion study of $(La_{0.60}Sr_{0.40})_{0.99}FeO_{3-\delta}$ disk
- Neutron diffraction and modeling study of phase stability, oxygen defect.
- Scheduled study of $La_{0.60}Sr_{0.40}Fe_{0.85}Ga_{0.15}O_3$ in task 4.
- Preparing samples to be sent to UIC.
- Expand the preparation of dense films on porous substrate studies.

TASK 5: Assessment of Microstructure of the Membrane Materials to Evaluate the Effects of vacancy-Impurity Association, defect Clusters, and Vacancy Dopant Association on the Membrane Performance and Stability

Professor Niegel Browning, University of Illinois, Chicago Circle

Results

In the last quarter we concentrated on the microstructural analysis of $(La,Sr)FeO_{3-}$ membrane material. For this study we used Praxair powder, which were then prepared and sintered at 1250° C by the group at University of Missouri, Rolla. After this process one sintered die spend 27 h at 750° C in an oxygen partial pressure of $P_{O_2} = 10^{-2}$ Pa. The first set of Z-contrast images and EEL spectra were acquired from this sample at room temperature after the reduction process. Figure 1a shows a Z-contrast micrograph, which exhibits the previously observed ordered change in contrast (see markers in the image). These changes in contrast, as previously shown, can be attributed to a brownmillerite-like ordering of oxygen vacancies in every second column. The chemically sensitive Z-contrast micrographs allow us to locate the electron probe very accurately to acquire bonding sensitive spectra from the iron-oxide columns in the bright and dark features. From atomic resolution EEL spectra we can then calculate the corresponding Fe valence for every column separately. As the iron L_3/L_2 white line ratio is very sensitive to the valence changes, it can therefore be used to determine the number of lower valence atoms, and the total intensity of the oxygen K-edge (when normalized to the iron intensities) will determine the amount of missing oxygen atoms. Our results show that the dark columns represent the reduced valence columns (Fe valence +2.6), whereas in the bright columns the valence is close to +2.8. The results show that in the dark FeO_2 lines the point-defect concentration is higher, because its reduced average iron valence indicates an increased number of vacancy clusters. It has to be stated that although we observe columns of ordered vacancy clusters, the contrast variations seem to be oriented in a random fashion and do not form large micro domains. The different lines also seem to penetrate each other forming a complex network of oxygen conducting channels

The $(La,Sr)FeO_{3-}$ sample was then heated in the microscope at an oxygen partial pressure of $P_{O_2} = 5*10^{-8}$ Pa to 451° C and stabilized for 12 hours. The contrast changes (figure 1b) appear more distinct in the sample, and can be clearly identified in the power spectrum of the acquired image (figure 1c). We can now observe small micro-domains of 8-16 unit cells width; the orientations and boundaries seem to be random. Note that the EEL spectra at elevated temperatures from the dark and the bright FeO_2 columns (figure 2), normalized to the intensity of the La M-edges, display different fine structures and intensities of the O K- and Fe L-edges. Also the Fe white line intensity ratios reveal a reduction of the transition metal valence from $+(2.8 \pm 0.1)$ in the bright to $+(2.3 \pm 0.1)$ in the dark columns respectively.
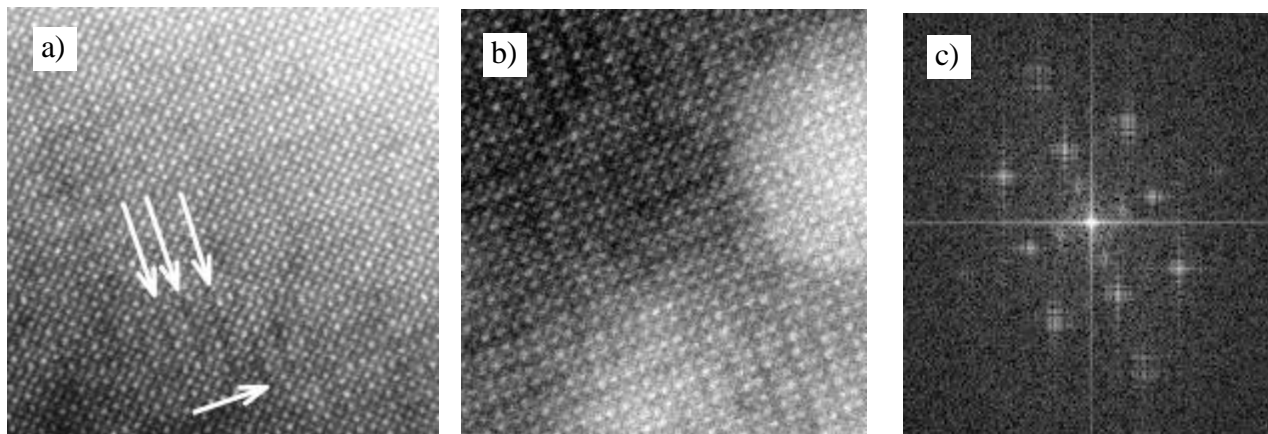
Figure 11: a) Z-Contrast image with marked change in contrast in every second FeO_2 column.
b) Z-Contrast image of (La, Sr)FeO_3 at 451° C with clearly visible ordered domain
c) Diffraction pattern showing additional spot at half distance between allowed reflections.

The sample was heated further to a final temperature of 801° C and kept under this condition for 3 hours. Due to the vibration introduced into the specimen holder by the water recirculation system at these temperatures we had to decrease the sample temperature to 451°C in order to resolve atomic structures. The Z-contrast image of sample after heating it to 801° C is shown in figure 3. Here the ordered domains, as well as the interwoven domain-boundaries can be seen very clearly. The picture suggest that the size of the micro domains is increased dramatically in this environment, and also the domain boundaries are more clearly defined after the increase in temperature. The stronger distinction between the reduced and the fully occupied atomic columns, suggests that the oxygen concentration in the dark lines is even lower than before. An analysis of the acquired EEL spectra at 451° C reveals that the already reduced, dark columns have an even lower iron valence of +(2.0± 0.1), whereas the bright columns remain at a constant valence of +(2.9± 0.1).
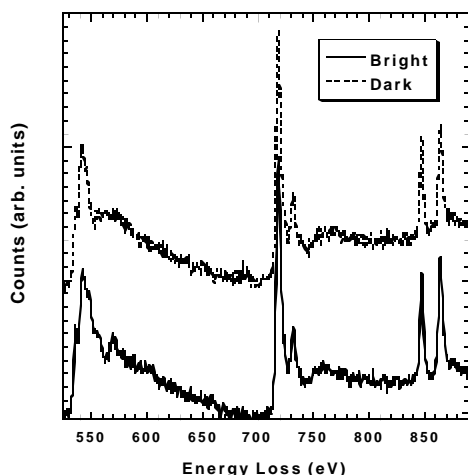

Figure 12: EELS of bright and dark columns in (La.Sr)FeO_3 at 451° C

A second disc of sintered, but untreated material was heated to 800° C in $P_{O_2} = 1*10^{-10}$ Pa until a stable equilibrium with its surrounding was reached. The image from the sample at room temperature (figure 3b) displays some features that were not observed in this sample before. Two dark lines of one unit cell width, separated by one bright line in the center (see inlet in figure 3b) are oriented along the [010] direction. Those lines mostly cross the whole grain, but some spontaneously start in the middle of the bulk. A closer look at those dark lines reveals that this structure is composed of a double layer of smaller contrast material, possibly FeO_2 whereas the center seems to consist of a monolayer of regular $(La,Sr)FeO_3$. The EEL data (figure 3c) acquired from the dark feature and from the surrounding bulk material are evidence that indeed these dark lines are caused by a stacking fault, as the La M-edge intensity is nearly halved in these columns. The different atomic environment in the stacking fault gives also rise to the observed difference in the O K-edge fine structure. Parallel to these stacking faults the reduced columns form huge domains in this kind of sample. In general, the ordered domain size is dramatically increased in this sample, but so far no other phases, such as $LaFeO_3$ or SrO could be found.
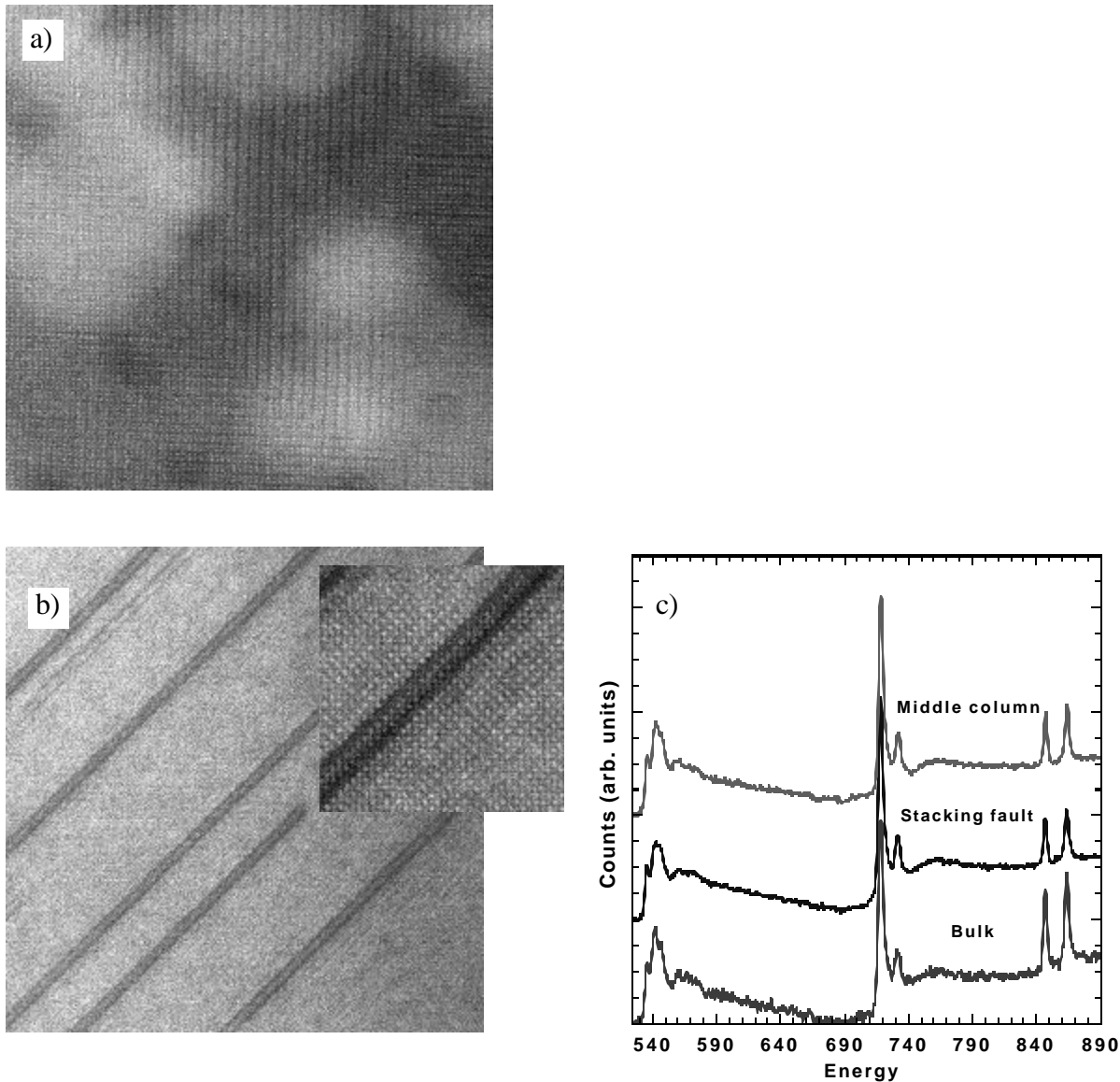

Figure 13: a) Z-contrast image of sample after heating to 801° C clearly showing the extended microdomains
b) Z-Contrast image of $(La,Sr)FeO_3$, previously treated at 800° C in 10^{-10} atm showing stacking faults and ordered structures.
c) EELS of $(La, Sr) FeO_3$ from bulk and stacking fault, normalized to oxygen and iron core loss edge.

Preliminary comparison between this results and conductivity measurements acquired at other group indicated that the observed microstructural changes can explain some of the unusual behavior of the conducting membranes under highly reducing conditions. However further correlation between the structural, conductivity and also mechanical property experiments will show the influence that these ordered domains and defects exert on the overall performance of the material.

Both samples were initially reduced at MIT in the group of Professor Tuller.

Task 6: Measurement of Surface Activation/Reaction rates in Ion Transport Membranes using Isotope Tracer and Transient Kinetic Techniques.

Progress during past 3 months at the University of Toronto

(1) Oxygen isotope infusion under gradientless conditions.

In this period we have given further consideration to measurements under reducing conditions using CO_2/CO to establish conditions characteristic of the reducing side of the membrane reactor. As we discussed at the last meeting, the WGS equilibrium is not achieved and complications arise from the extremely rapid exchange of CO_2 with the surface. This has been reported for other oxides. Rapid exchange is advantageous in that it assures that sufficient oxygen is infused for proper measurement of the diffusion coefficient. This exchange process, shown schematically in the left of the scheme below, presumably takes place through a carbonate intermediate and does not represent a redox process involved in net oxygen transport across the surface. In contrast, the rate of the reverse water gas shift reaction gives some indication of the rate of the redox process indicated on the right hand side of the scheme. Both redox of surface sites and water gas shift are involved in the exchange. The contribution from the redox process can be determined by measurement of the labelled CO in the gas phase.

scheme
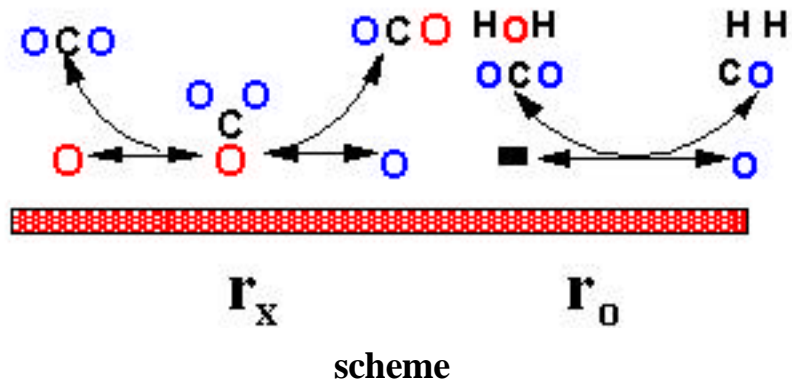
We have developed a model that includes both surface rates in addition to bulk diffusion appropriate for our reactor geometry. The results from one set of data and comparison with the model calculation are shown in Figures 1 and 2. Figure 1 shows the evolution of the ^{18}O fraction with time in the gas phase as determined by mass spectroscopy. Figure 2 shows the isotope depth profile in the sample of $La_{0.2}Sr_{0.8}Fe_{0.8}M_{0.2}O_{3-x}$ used. The experiment was carried out at 850ºC.
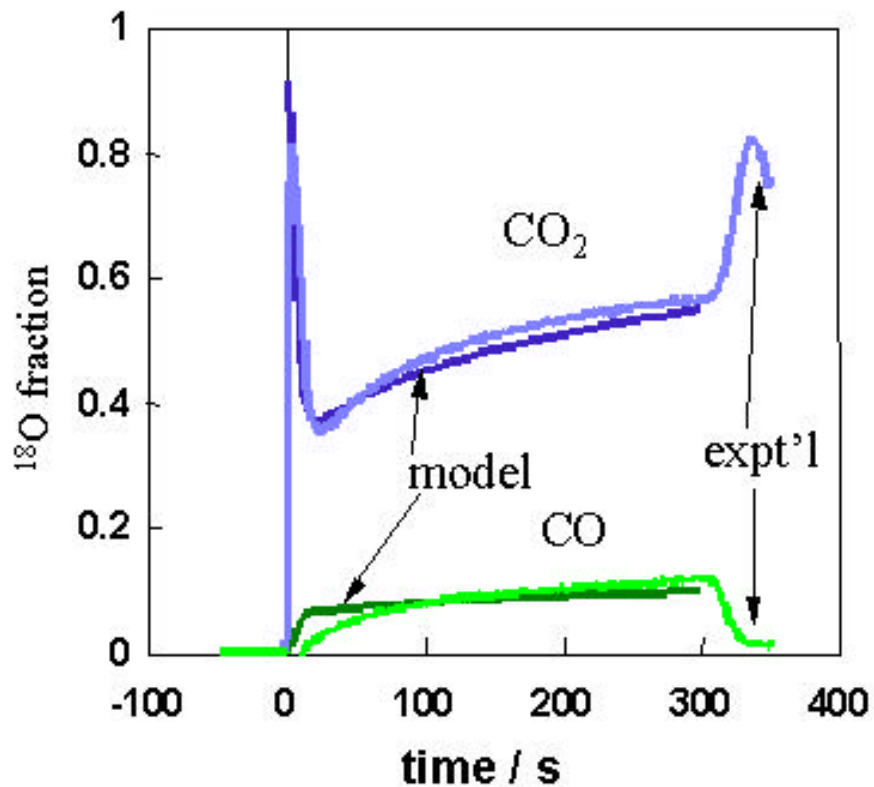
Figure 1.   The data and model predictions for the ^{18}O distribution between CO and CO_2.

5
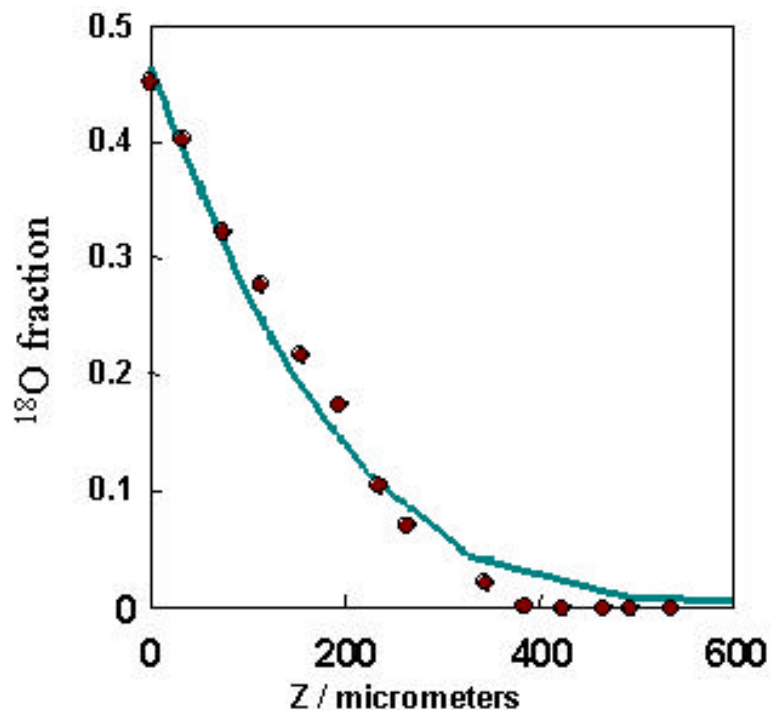
Figure 2 ^{18}O isotope depth profile in the solid

From the analysis of the data the values of the oxygen diffusion coefficient and the two surface exchange rates are obtained as shown in Figure 3. In fact under the conditions of the present experiment the non-redox exchange process is too fast to measure and so the value of k_x cannot be determined. The rate of the redox process can be determined, however, and is shown for comparison with the O_2 exchange rate k^* previously measured in Figure 3. To the best of our knowledge this is the first measurement that enables the separation of the two exchange mechanisms.   The oxygen diffusion coefficients measured at the two partial pressures differ by a factor of three. Some of the difference arises from the difference in the vacancy concentration under the two conditions but this requires further study.

All the parts for the membrane reactor have been received and initial assembly and shakedown of the reactor is will begin in the next quarter. As described in the previous report, the membrane reactor is a tubular design, rather than the initial design to use disc-shaped membranes. Tension is held on the seals by a bellows fitting at the end of the reactor.
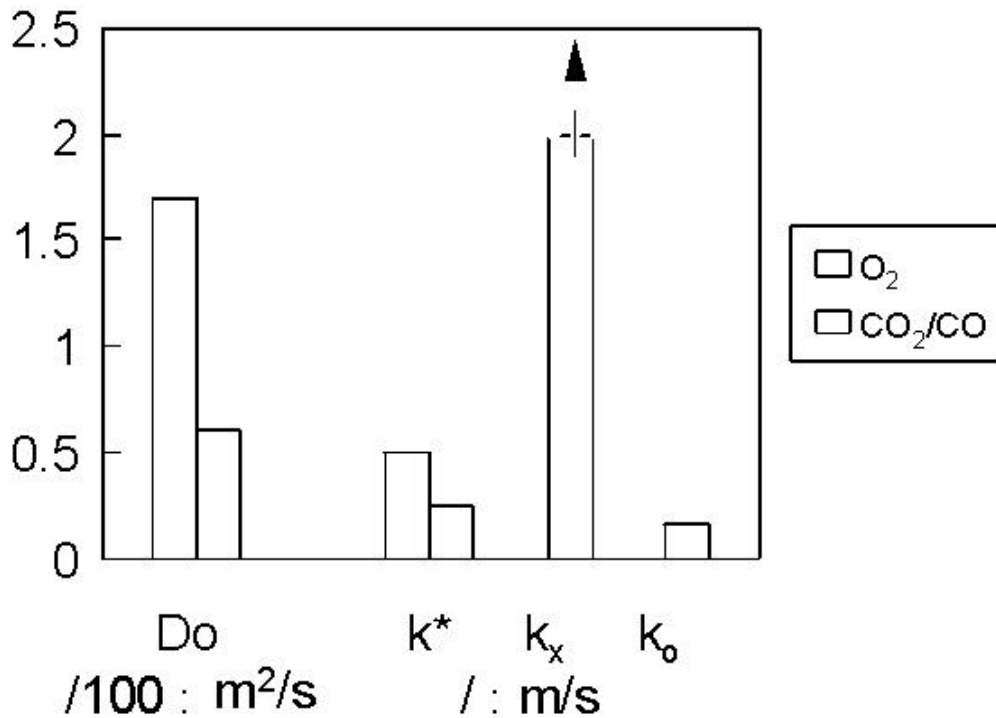
Figure 3   Comparison of D and k values obtained in oxygen and CO/CO$_2$ mixtures

(2) Transient oxygen isotope infusion in operating membrane reactors.

Progress during the last 3 months at UH

(1) Conductivity and Stoichiometry of **La$_{0.2}$Sr$_{0.8}$Fe$_{0.8}$M$_{0.2}$O$_{3-x}$**.

Most of our effort in the last three months has involved measurements of the conductivity and stoichiometry of **La$_{0.2}$Sr$_{0.8}$Fe$_{0.8}$M$_{0.2}$O$_{3-x}$** in sealed cells of the type shown in the Figure. We have
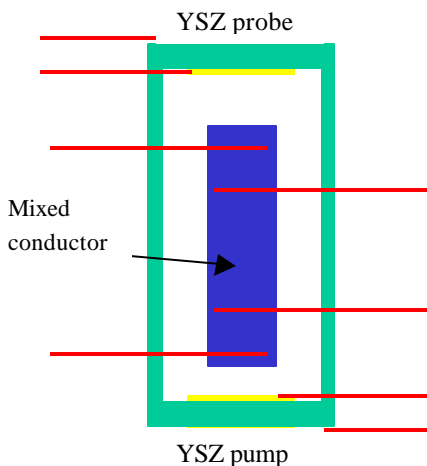
used a four probe ac technique to measure the conductivity at temperatures from 750ºC to 1060ºC in oxygen partial pressures from 0.2atm to 10^{-20}atm.

Thermodynamic and conductivity data are required for interpretation of the chemical diffusion and exchange measurements to obtain values of D and k that are used to guide the infusion studies. We are also using a lock-in amplifier ac technique in order to measure very small changes in the resistance of the sample. The first set of electrical conductivity results for one system is shown below

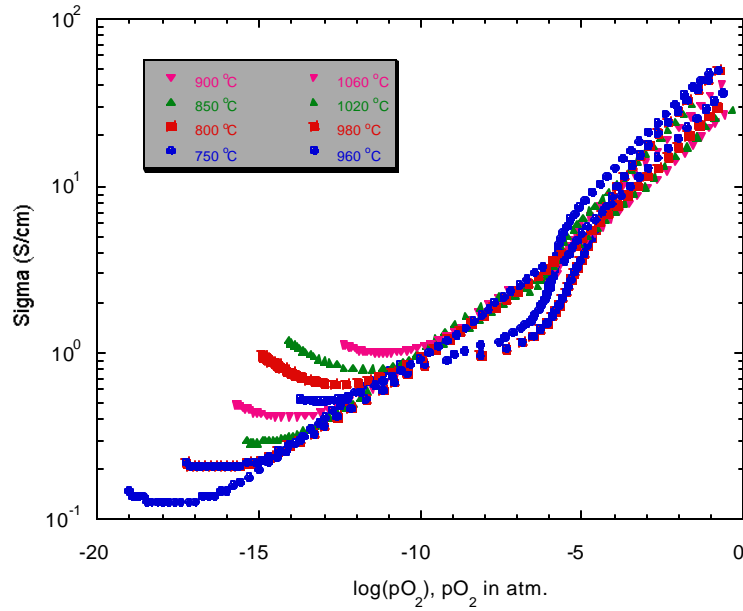in Figure 4 for eight temperatures.
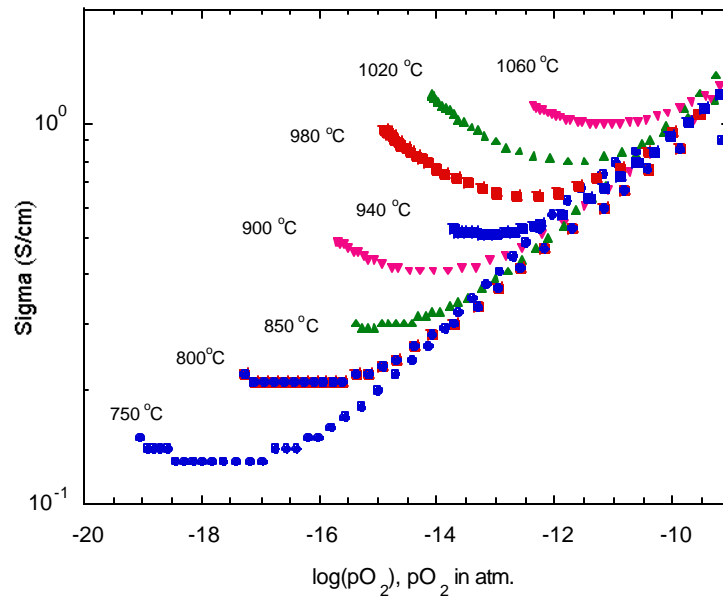
7

Figure 4 Conductivity Data for $La_{0.2}Sr_{0.8}Fe_{0.8}M_{0.2}O_{3-x}$

Figure 5.   Low Pressure Conductivity Data for $La_{0.2}Sr_{0.8}Fe_{0.8}M_{0.2}O_{3-x}$

The data show p type conductivity at high oxygen partial pressures as expected. At low partial pressures a transition to n-type behavior is observed.   At the highest temperature the transition from p to n type behavior is smooth but at lower temperatures there is evidence for the formation of an intermediate phase presumably as a consequence of vacancy ordering. The low-pressure data are shown in more detail in Figure 5.

If it is assumed that at the minimum in the conductivity data the electronic contributions are negligible and the conductivity is primarily ionic, the temperature dependence of the ionic conductivity can be obtained as shown in Figure 4. The measured conductivity is in the range of 0.1 to 1 S/cm over the temperature range measured. Further analysis of these data will be carried out in the next period and comparisons will be made with results on other samples and obtained by different groups. We will also check the reproducibility and the reversibility of the present data and investigate further the origin of the intermediate behavior below about 10^{-5} atm. We will also quantify the stoichiometry measurements.
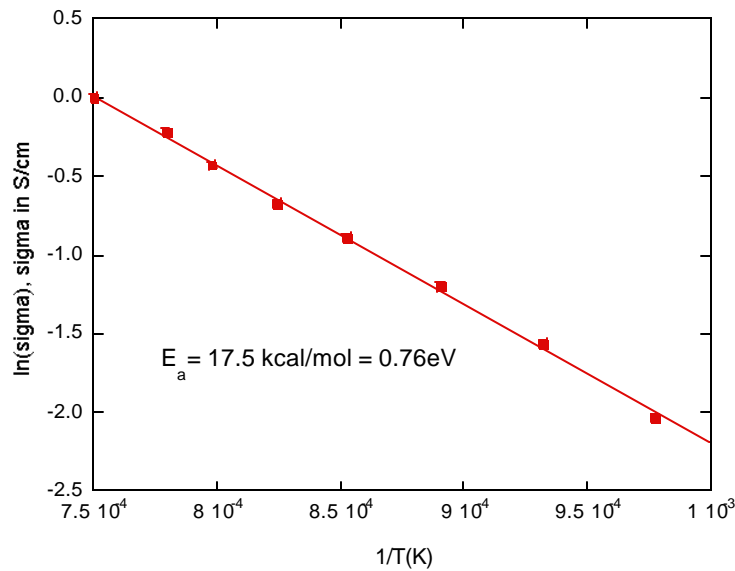

Figure 6 Ionic conductivity of $La_{0.2}Sr_{0.8}Fe_{0.8}M_{0.2}O_{3-x}$

(2) Materials

In order to carry out the isotope transient/membrane experiments at UT, we need to fabricate tubes of the appropriate dimensions. We began with $La_{0.6}Sr_{0.4}Fe_{0.8}Co_{0.2}O_{3-x}$ as the material and will also make $La_{0.2}Sr_{0.8}Fe_{0.8}M_{0.2}O_{3-x}$ tubes in the future. We will use the sintering protocol that we have developed to fabricate rods and discs rods.

DOE Tasks for next 3 months University of Houston

(1) We will continue the electrical conductivity relaxation measurements on $La_{0.2}Sr_{0.8}FeO_3$ to resolve the observed anomaly and complete the measurements on $La_{0.2}Sr_{0.8}Fe_{0.8}M_{0.2}O_{3-x}$.

(2) Additional tubular and disk samples of $La_{0.2}Sr_{0.8}Fe_{0.2}M_{0.2}O_{3-x}$ will be prepared and characterized for transient membrane studies and isotope infusion.

(3) We will quantify the stoichiometry changes in $La_{0.2}Sr_{0.8}Fe_{0.2}M_{0.2}O_{3-x}$ and verify the reproducibility and reversibility of the data.

DOE Tasks for next 3 months University of Toronto.

(1) ^{18}O infusion in ferrites in gradientless conditions.

 (a) The analysis of the profiles obtained in this quarter will be completed,

 (b) Further examinations of the oxygen transport in $La_{0.2}Sr_{0.8}Fe_{0.8}M_{0.2}O_{3-x}$ under reducing conditions will be performed. We will use C^*O_2/CO mixtures for the infusion, thus establishing a defined oxygen potential, but allowing measurement of the redox process by being able to follow the extent of isotopic equilibration between CO and CO_2 in the mass spectrometer.

 (c) Additional infusions in air will be performed to extend the temperature range on the ferrites above and repeat several of the conditions. We will study two new samples recently provided.

(2) Operating membrane experiments

 (a) A new staff member will start the initial shakedown experiments. The initial assembly uses a dense alumina or quartz tube in place of the membrane. This will allow shakedown of the system without risking the perovskite tubes and proved rigorous leak-check to validate the seals. If all goes well, we will then start oxygen permeation measurements (with no reductant on the fuel side) towards the end of the period with the $La_{0.6}Sr_{0.4}Fe_{0.8}Co_{0.2}O_{3-x}$ tube currently available.